Reconstruction and Filtering of Vascular Structure in 3D Photoacoustic Microscopy

	Israr Ul Haq
	Tohoku University
	11301　17800
URL	http://hdl.handle.net/10097/00125072

Tohoku University

Graduate School of Biomedical Engineering
Graduate School of Biomedical Engineering, Biomedical Imaging Laboratory

B4WD9001

Reconstruction and Filtering of Vascular Structure in 3D Photoacoustic Microscopy

Candidate
Israr Ul Haq

Supervisor
Prof. Yoshifumi Saijo, M.D., Ph.D.

Advisors
Prof. Shin-ichiro Umemura, Ph.D.

Prof. Yuji Matsuura, Ph.D.

2014-2017

Tohoku University, Graduate School of Biomedical Engineering, Biomedical Imaging Laboratory.

To my Family.

Acknowledgments

Abstract

Medical diagnosis has been playing a key role for the early grading of many diseases. Different imaging modalities have been used for diagnosis. In this research reconstruction and filtering of vasculature in Three-dimension (3D) optical resolution photoacoustic microscopy (OR-PAM) is analyzed. Quality of photoacoustic (PA) images is degraded due to different parameters such as frequency or diameter of the transducer while data acquisition. Reconstruction and denoising of photoacoustic images is an important issue to diagnose diseases at early stages. In the proposed method raw photoacoustic images acquired by OR-PAM are first pre-processed and denoised using sparse based representation and then filtered using Wavelet and Hessian based method. The vascular structures are enhanced by the wavelet filtering and 3D tubular structures are classified by the eigenvalues of the Hessian matrix. The eigenvalues of the Hessian matrix were used for the detection of bifurcation point. Symmetric analysis of eigenvalues were considered to detect these junction points. The algorithm is tested on PA images of human finger cuticle, vasculature in mouse and on phantoms. The results reveal better denoising and filtering capability of PA images. The proposed methods were tested on two-dimension (2D) and 3D data for validation.

Abbreviations

1D: One-dimensiondal
2D: Two-dimensional
3D: Three-dimensional
PAM: Photoacoustic Microscopy
OR-PAM: Optical resolution photoacoustic microscopy
AR-PAM: Acoustic resolution photoacoustic microscopy
PA: Photoacoustic
CT: Computed Tomography
MRI: Magnetic Resonance Imaging
PET: Positron Emission Tomography
K-SVD: K-means singular value decomposition
MAP: Maximum amplitude projection
MIP: Maximum intensity projection
B-mode: Brightness mode
FFT: Fast Fourier Transform
PSNR: Peak signal-to-noise ratio
SNR: Signal-to-noise ratio
ANSI: American National Standards Institute

Contents

List of Figures

Chapter 1

Introduction

An increasing in population leads to an increased in necessity for early medical diagnosis. Several imaging modalities such as X-ray, Computed Tomography (CT), Magnetic Resonance Imaging (MRI), Positron Emission Tomography (PET) and Ultrasound have been widely used for the diagnosis and treatment of internal organs and vessels in clinics. In this research we used OR-PAM to analyze the vascular structures in human and animals. In most of the cases medical data contains noise during data acquisition. Such data is difficult to visualize and small structures are difficult to discern from background in the data. Blood vessels are of particular interest for clinical studies [8]. Clear visualization of blood vessels is crucial for the early diagnosis of cardiovascular diseases, Thrombosis, Inflammation, Vascular occlusion, Aneurysm, Embolism [43] and other vascular diseases. To visualize blood vessels the imaging modality should be capable of acquiring blood vessels of different sizes. In this research we used OR-PAM to acquire the vasculature under the skin non-invasive, which is a 3D imaging modality.

OR-PAM is an emerging optical-acoustic hybrid imaging modality capable of imaging at sub cellular level with high resolution and sensitivity [27]. It has been used for imaging of tissues by optical absorption of hemoglobin. In PAM a short-pulsed laser is used to illuminate the target object. The absorption of light results in the rise of temperature, which subsequently results in pressure rise via thermoelastic expansion of the tissues. Due to this thermoelastic expansion acoustic signal propagates, which is detected by the ultrasonic transducer to form the image of absorption source [84]. In PAM the axial is given by $0.88c/\Delta f$, where c is the speed of the sound in the tissues which is considered constant (around $1500\,\mathrm{m/s}$) and Δf is the frequency bandwidth of the transducer [77,78]. The axial resolution depends mainly on the frequency of the transducer. In OR-PAM the lateral resolution is given by $0.51\lambda/NA$, where λ is the wavelength, and NA is the numerical aperture of the optical objective [76]. The acquired 3D data requires reconstruction and filtering for clear visualization of blood vessels.

1.1 Anatomy of blood vessels and skin

The skin is divided into three layers:

Epidermis : It is the outermost layer of the skin, provides protection to the inner layers from germs and makes it difficult for bacteria and viruses to enter in the body.

Dermis: It is a thick layer of fibrous and elastic tissues below the epidermis containing sweat glands, hair follicles, nerve endings and blood capillaries.

Hypodermis: Hypodermis is the deepest section of the skin. It consists of loose connective tissues and lobules of fat. Larger blood vessels and nerves are found in hypodermis.

Fig. 1.1 shows the different layers of the skin. The blood vessels are part of the circulatory system and found in the dermis and hypodermis layer of the skin. There are three major types of blood vessels. Arteries : Carry blood away from the heart. Veins: Carry blood back to the heart from different body parts. Capillaries: These are the smallest of body's blood vessel ranging from 5 to 10 micrometers in diameter and help to exchange oxygen, water, waste substances, and other nutrients between the blood and the tissues [48]. Fig. 1.2 shows the arteries, veins and capillaries. The recent emergence in photoacoustic imaging provides a promising solution for optical absorption imaging.

1.2 Photoacoustic imaging

Photoacoustics provides a precise way to imaging blood vessels because of the capability of photoacoustic to resolve optical absorption in biological tissues. This leads to new branch of photoacoustics called PAM. In PAM imaging sensitivity is maximized by optical excitation and ultrasonic detection. In case of acoustic resolution photoacoustic microscopy (AR-PAM) deep tissue imaging is achieved by tight acoustic focusing and weak optical focusing. To examine the anatomy and function of tissues at cellular or sub-cellular level AR-PAM is considered inadequate. To fill this gap OR-PAM is considered superior at resolving optical absorption at cellular level. In case

of OR-PAM optical focus predominates the acoustic focus to improve the lateral resolution of PAM at the cost of imaging depth [47]. Thus in OR-PAM it is difficult to imaging at deeper part and in case of scanning mouse OR-PAM requires scalp to be removed, while AR-PAM can image vessels by penetrating the scalp and skull [46, 80]. To excite the tissues, hemoglobin in the red blood cells play a vital role to visualize blood vessels. At 532 nm, there is high absorption of hemoglobin and melanin. At this wavelength light cannot penetrate as deeply as some other wavelengths but green light gets absorbed by the hemoglobin in the dermis layer. For diagnosis and treatment of deeper vessels this wavelength is not suitable because of scattering. The light absorbed by the tissues generates an initial pressure rise due to conversion into heat. The Grüneisen parameter of tissue is usually determined by fitting the photoacoustic spectra and measured in a wavelength range in which the absorption coefficient of the tissue is much greater than its reduced scattering coefficient [71]. Few methods have been proposed for Grüneisen parameter of tissue [58]. Measuring of Grüneisen parameter using interferometric method [64], in which they measured the sample surface displacement by the thermal expansion due to light absorptions. Grüneisen parameter of blood by photoacoustic method was measured in [58]. The generation and detection of pressure wave is a complicated process, the measurements can be made quantitative only be calibrating the measuring system with homogeneous media that have well-known Grüneisen parameter but this is not always the case as Grüneisen parameter also depends on the optical and mechanical parameters of the medium. The Grüneisen parameter Γ of tissue is proportional to the initial pressure p_0 to the light absorption as shown in

Eq. 1.1

$$p_0 = \Gamma\mu_a F, \qquad\qquad (1.1)$$

where μ_a is the absorption coefficient of tissue and F is the light fluence and is determined by the optical absorption and optical scattering between sample surface and absorber. The Grüneisen parameter vary between the same type of tissue. For example, Grüneisen parameter of blood is estimated to be 0.152 and 0.226, which causes uncertainty in the photoacoustic imaging [58].

Variety of chromophores can be identified by their unique absorption spectra shown in Fig. 1.3. Deoxyribonucleic acid (DNA) and ribonucleic acid (RNA) show strong absorption in the ultraviolet region and has been used for the imaging of cell nuclei [29]. In the visible region, hemoglobin has a strong absorption spectra and has been used to visualize blood vessels and to study angiogenesis and oxygen concentration in blood [26, 50]. The ultraviolet, visible and near infrared region have strong absorption of melanin. It is an important biomarker for cancer [76]. For the quantification of oxygen saturation (SO2), spectra of oxy-hemoglobin (HbO2) and deoxy-hemoglobin (HbR) overlaps, in such case spectral decomposition is necessary [29].

1.3 Photoacoustic waveform

The photoacoustic signal has a useful information regarding the dimension, geometry, density of the irradiated body can be found from the shape of the
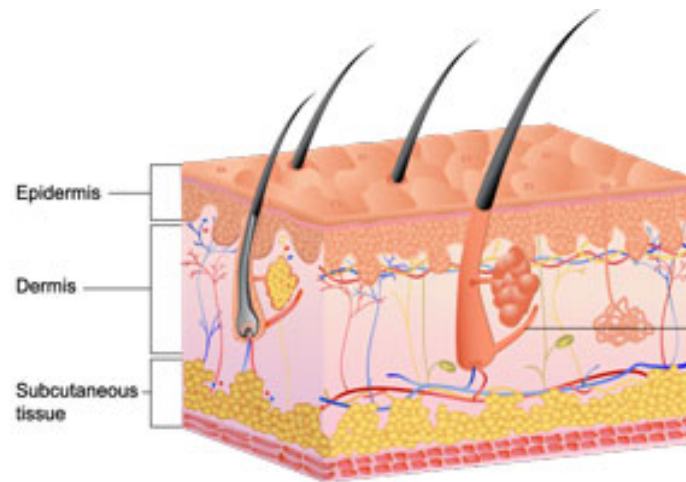
Figure 1.1: Epidermis, dermis and hypodermis.
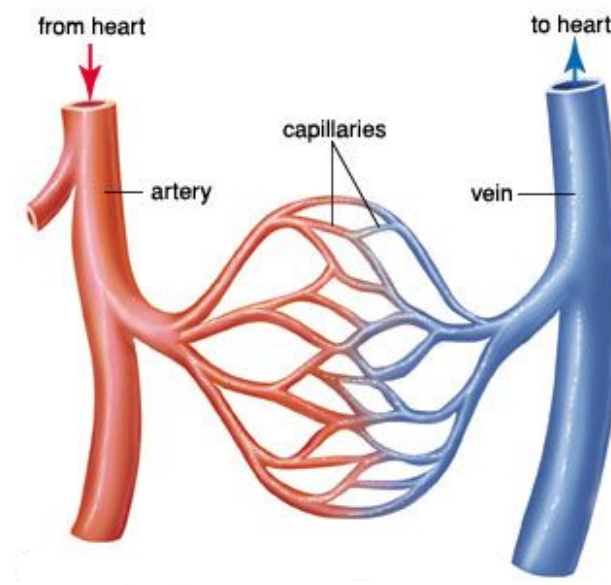
Figure 1.2: Arteries, veins and capillaries.

PA waveform. The information can be used precisely to know the physical characteristics of the irradiated body [15]. Three structures were considered for short laser pulse case; a thin layer of fluid, a fluid cylinder and a droplet
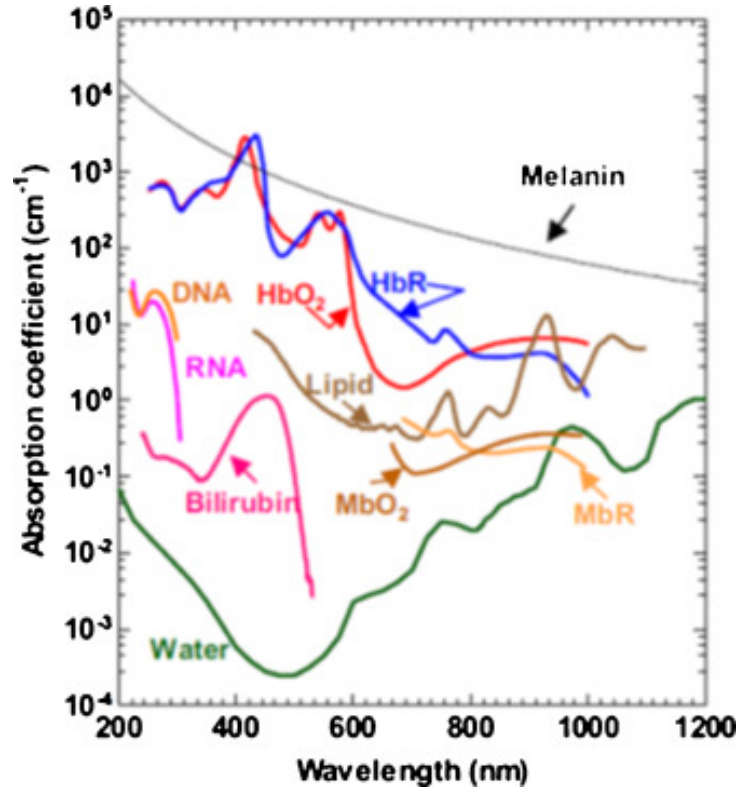
Figure 1.3: Optical absorption spectra.

for spherical case. Diebold *et al.* showed that one, two and three dimension of long laser pulses is proportional to zeroth, one half and the first derivative respectively. In this research a fluid containing cylinder is assumed to be as a blood vessel [16,34]. Figure 1.4 shows the photoacoustic waveform which is close to the waveform discussed in [15], the diameter of the vessel is around 30 µm.
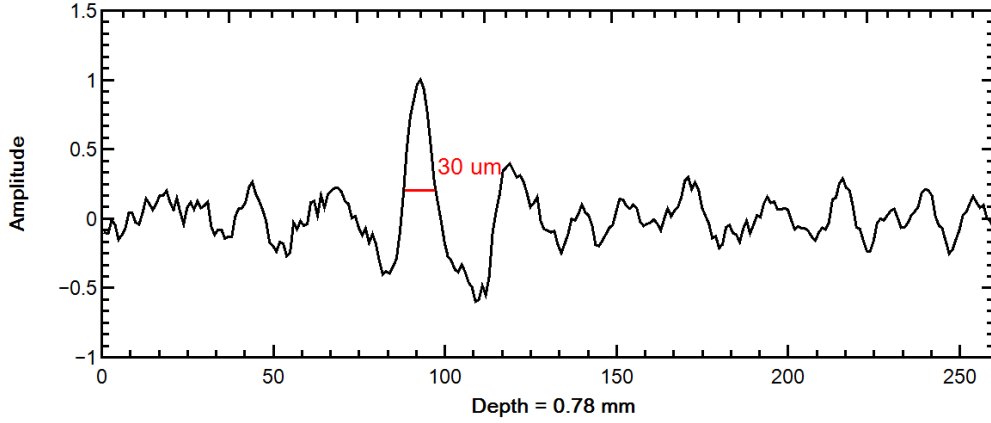
Figure 1.4: Photoacoustic signal from mouse blood vessel.

1.4   Experimental setup

In OR-PAM the laser beam is focused by objective and two prisms are sep-
arated with a thin layer of silicon oil under the objective and correction lens
which is used to align the optical excitation and acoustic detection. The
schematic diagram of OR-PAM is shown in Fig. 1.5. The OR-PAM system
with laser wavelength of 532 nm, pulse duration 8 ns and pulse repetition fre-
quency (PRF) of 5 kHz was used to irradiate tissues (Micro Photo Acoustic
Inc. in NY ,USA) and (Advanced Optowave Corporation, NY, USA). The
ultrasound with center frequency of 20 MHz and sampling rate of 500 Mbps
was used to acquire PA image. The maximum lateral and axial resolutions of
the system are 5 μm and 15 μm respectively. The maximum imaging depth
of the system is 1 mm, below this limit the incident light undergo scattering
which jumbled up the light path and inhibits effective optical focusing. The
image contrast is based on optical absorption, which shows that technique
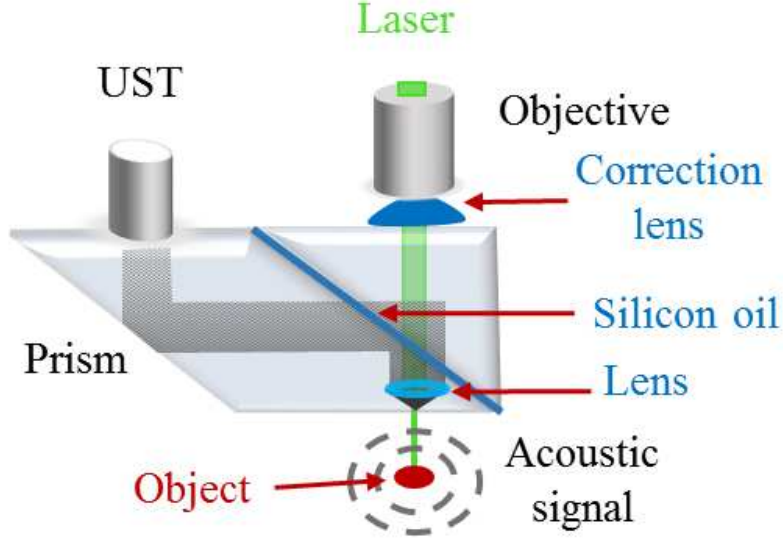
Figure 1.5: Schematic of OR-PAM.

is well suited to visualize blood vessels due to strong optical absorption of hemoglobin. Since, HbR and HbO_2 are two major sources of optical absorption in tissues and PAM is well suited to image blood vessels within the spectral region [38,62]. Each laser pulse produces one A-Line which is one-dimensional (1D) depth resolved image. The volumetric image is acquired by 2-D raster scanning of ultrasonic transducer along the transverse plane [28,72,81]. The B-scan rate for a 2-mm line is 5 Hz with 0.625 µm step size. If the ultrasonic detector with high central frequency, large numerical aperture and bandwidth is employed, the PA source can be visualized with high spatial resolution [79].

The data acquired from mouse ear; A healthy mouse with hair removed is used to acquire 3D vascular image. Fig. 1.8 shows the mouse with hair removed, the total length of the mouse was approximately 10 cm. Fig. 1.6

Figure 1.6: Mouse for data acquisition.

shows the ear of a mouse containing vascular structure. The raster scanning on mouse ear is shown in Fig. 1.7. In this research a laser with a wavelength of $532\,\mathrm{nm}$ is used for all the experiments. All the parameters for Gabor wavelet and Hessian based methods used in this research are tuned for photoacoustic images. These parameters need to tune again if the image modality is changed.

Figure 1.7: Mouse ear for data acquisition.
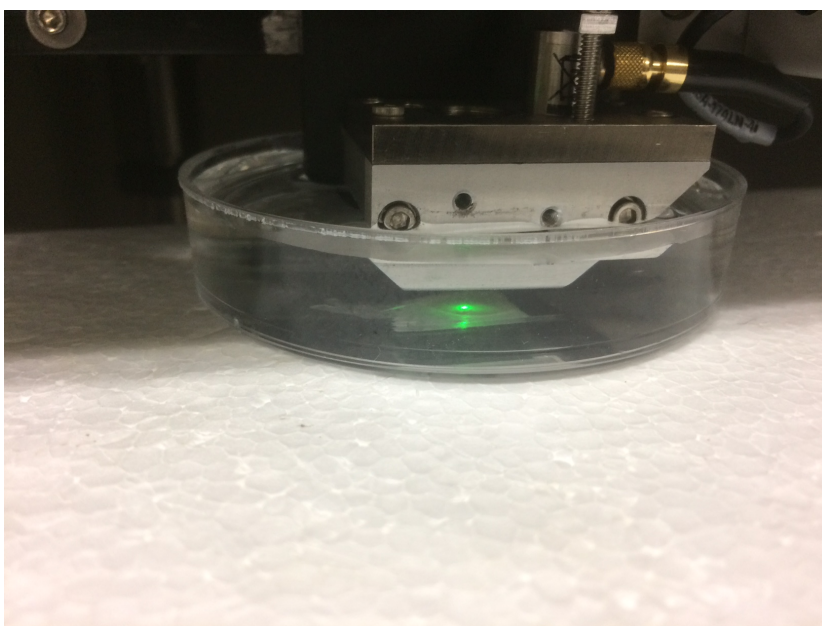
Figure 1.8: Raster scanning of mouse ear.

Chapter 2

Problem formulation and proposed method

This chapter describes the importance and novelty of the algorithm in medical imaging. In the first part of this chapter, literature is reviewed about the techniques of denoising, reconstruction of vessels and bifurcation points in photoacoustic images, while the second part describes the problem formulation and the third part shows the complete flow diagram with explanation of the proposed technique and contribution of the proposed method is discussed in the end of this chapter.

2.1 Literature review

A number of methods have been proposed for vessel enhancement. In this section the most widely used methods are reviewed. Vessel segmentation us-

ing window-based technique was proposed in [52]. They used the X-ray image of artery to estimate the diameter and cross-sectional area at each point along the artery. Vascular structure segmentation using energy-minimization problem was proposed in [41] where they used the zero level set and distance function to segment the vasculature. Another approach where it is assumed that centerlines of the vessels appear brightest and can be detected by considering them as intensity ridges of the image [4]. A differential geometrical approach in which the volumetric MRA image is treated as 4D hypersurface space whose extrema of curvature corresponds to vessel centerlines [53]. A statistical approach in which Gaussian intensity distributions are assumed for background and for vessel intensities and for threshold expectation maximization algorithm (EM) is applied to classification [65]. A filter for dot, line and plane like structures is proposed in [39], which can enhance objects of a specific shape and suppress objects of other types. An improved version of Hessian filtering in proposed in [70], in which the grayscale factor is added to the vascular similarity function computed by Hessian matrix eigenvalue. Their method is experimented on brain MRA data and lung CTA data.

Active models [2, 40] and center-line extraction [5, 63] for vessel filtering have low response at bifurcation points. Kumar *et al.*, [35] extracted the vascular structure using vessel cross-section area, the method uses the analysis of Hessian matrix. Schneider *et al.*, [61] proposed a 3-D vessel segmentation and center-line extraction based on multivariate Hough voting and oblique random forests. Azzopardi *et al.*, [6] proposed automatic detection of vascular bifurcations in a segmented retinal images by using combination of shifted filter responses. They calculated the response of their filter by the weighted

geometric mean of Gabor filters. Kerneki *et al.*, [33] proposed a method for bifurcation detection which is based on multiscale Hessian analysis, and use histogram of eigenvectors weighted by the vesselness measure. They claim that pixels with three peaks in their immediate neighborhood are considered as bifurcation candidates. McIntosh *et al.*, [49] proposed a vessel crawl based algorithm that crawls along the vessel to segment and exploring the bifurcation points. Zhou *et al.*, [83] proposed a method to detect the tubular structures based on eigenvalues analysis and for bifurcation detection they used adaptive boosting algorithm. Most of the proposed methods are based on Hessian based vessel filtering which use eigenvalues of the hessian matrix to classify vascular structures [20].

2.2 Problem formulation

Reconstruction of vasculature from medical images have been a major problem when it comes to diagnosis. The images acquired from different modalities have different properties in terms of noise and useful information in it. With the advent in modalities properties of noise change and new algorithms are of great interest. The noise in PA images acquired from OR-PAM are usually induced by laser light, ultrasonic parameters and scattering effect in the tissues. The reconstruction of vasculature in PA images plays a vital role for vessel study.

2.3   Proposed method

In the proposed technique we used 3D Gabor wavelet and Hessian based method to reconstruct the vascular structures. In the pre-processing step 3D data is first denoise with sparse representation using K-means Singular Value Decomposition (K-SVD). Further in the proposed technique vascular bifurcation points are detected in 3D data using eigenvalues of the Hessian matrix. The flow diagram of the proposed method is shown in Fig. 2.1. The flow diagram shows the main steps of the proposed methods to denoise PA images.

1. **Pre-preprocessing**

   (a) The PA image is first input to the pre-processing block, at this stage if the image is too big it can be downsampled to decrease the computation time at the cost of losing some information. The downsampling results in decreasing the resolutions of the image; small and thin vessels may disappear in result of downsampling.

   (b) The downsampled image is bandpass filtered to remove the high and low frequency components to suppress the noise.

   (c) Median filtering is applied on bandpass filtered image to remove impulse noise. This block is further explained in chapter 3.

2. **Gabor wavelet**: It is used to enhance the effect of vasculature in each direction at multiscale level to enhance the effect of smaller and bigger vessels.

3. **Hessian based filtering**: It is used to classify and distinguish tubular structures from other structures. It is also a multiscale filtering to classify smaller and bigger vessels; further explained in chapter 5.

4. **Bifurcation point detection**: At this stage bifurcation points in 3D vasculature is detected. These branch points help to identify those points where Hessian based method fails to join vessels; further explained in 6.

5. **Sparse representation based denoising**: Sparse representation is used to denoise images. In this research, this method is used to denoise photoacoustic images. The method is further explained in chapter 4.

2.4 Contribution

The previously proposed methods are used to enhance the vasculature, but the proposed method consists of integration of Gabor wavelet and Hessian based method for vessel reconstruction and a novel method to detect the bifurcation points is discussed in detail. The contributions are as follow:

1. Vasculature reconstruction by adding directionality in the standard Hessian based method.

2. Reconstruction of 3D Gabor wavelet to add directionality for vessel enhancement.

3. Denoise PA images with sparse representation.
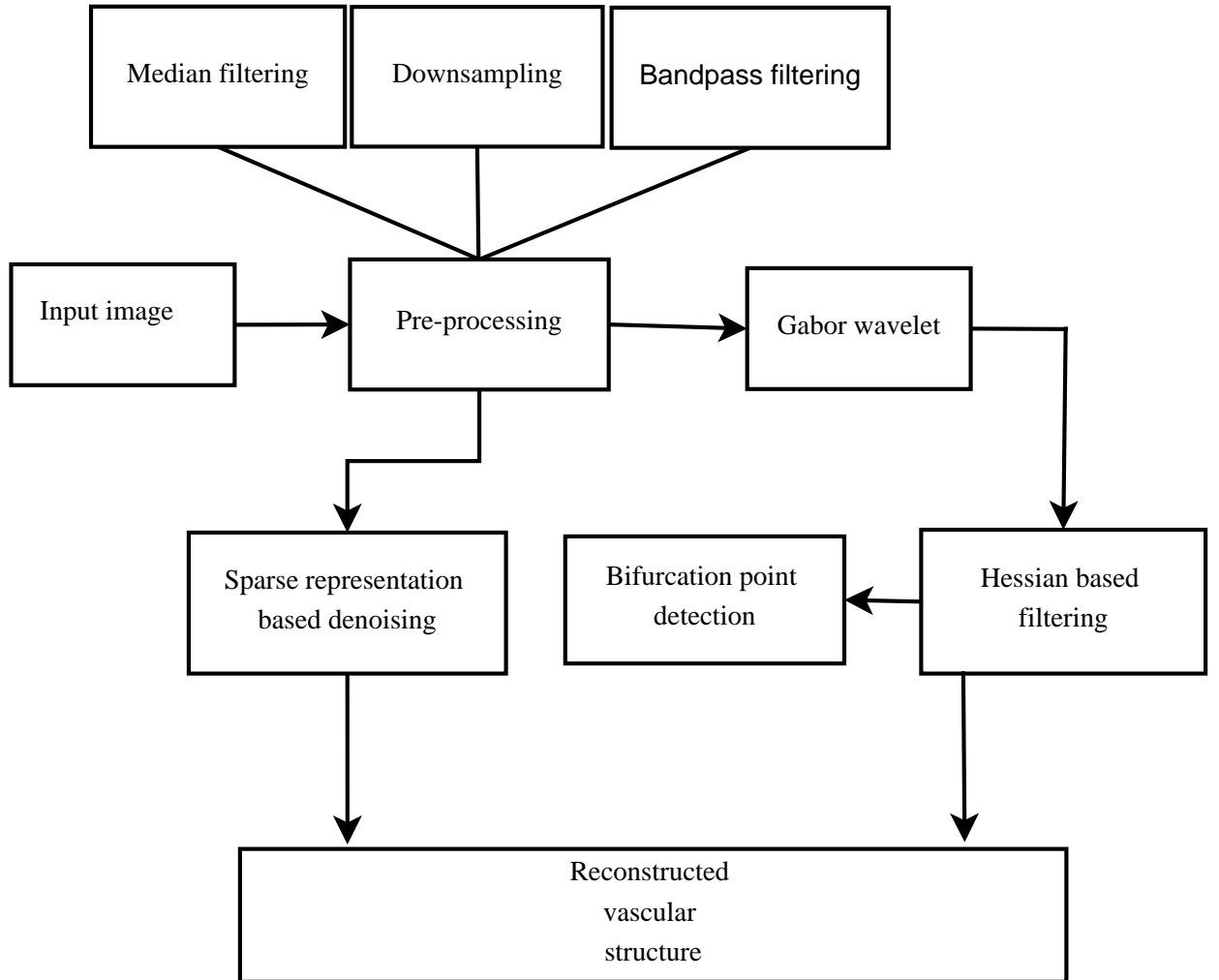
Figure 2.1: Flow diagram.

4. Novel method to detect bifurcation points by eigenvalues of the Hessian matrix.

2.5   Summary

In this chapter the previously proposed methods to reconstruct vasculature are discussed and flow diagrams of the proposed methods to reconstruct

vasculature are shown. The proposed method uses Gabor wavelet filtering to enhance vasculature, Hessian based filtering to reconstruct and sparse representation to denoise the PA images. The contribution of the research work in terms of novelty to denoise vessel is also described. The methods are discussed in detail in chapters 3, 5 and 4 respectively.

Chapter 3

Pre-processing of photoacoustic images

In this chapter we describe the composition of PA signal, the A-line, B-mode and Maximum Amplitude Projection (MAP) images. The pre-processing of PA images which includes the band-pass filtering around the center frequency of the transducer to remove very low and high frequency components. Then 3D median filtering is applied to remove impulsive noise from 3D PA volumetric data. Results of pre-processing on PA images are shown in the last section of this chapter. [1]

---

[1]The pre-processing steps discussed in this chapter published as one of the section in

Israr Ul Haq, Ryo Nagoaka, Takahiro Makino, Takuya Tabata and Yoshifumi Saijo, "3D Gabor Wavelet based Vessel Filtering of Photoacoustic Images", *The 38th Annual International Conference of the IEEE Engineering in Medicine and Biology Society*, Orlando, USA, Aug. 2016.2

3.1   Photoacoutic signal

Photoacoustic signal is a wide band signal which covers most of the frequency components. The acquired signal depends on the frequency of the transducer. High frequency transducers are suitable for better visualization of vessels at lower depth, whereas low frequency transducers are suitable for the visualization of deeper vessels. The acquired signal contains noise from the transducer and tissues. The 3D data acquired from the transducer contains A-line signal. The A-line signal acquired from human finger cuticle and mouse brain vessel is shown in 3.1 and 3.2 respectively. The signal contains the information of the diameter of the target sample as well. The 3D data is composed of many A-line signals and one slice of image is considered as B-mode. The B-mode image is shown in Fig. 3.4; the black hollow spots in the image show the blood vessels. The cross sectional view of whole 3D image is shown in Fig. 3.5. The first pre-processing step is to remove the low and high frequency components from the signal, to remove such components bandpass filter around the center frequency of the transducer is used for filtering. The magnitude response of the bandpass filter is shown in Fig. 3.3. The radio frequency (RF) signal is first filtered by the bandpass filter. The filtered image shows the removal of low and very high frequency components, whereas the noise can be seen in the original unfiltered bandpass filtered image as shown in Figs. 3.7 and 3.8 respectively.
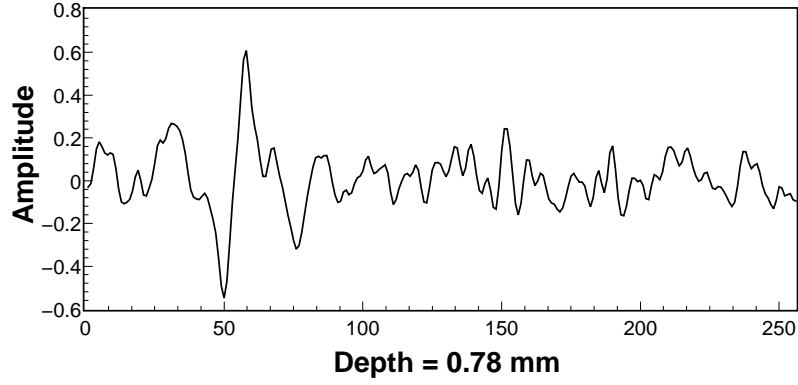
Figure 3.1: A-line signal from a vessel of human finger cuticle.
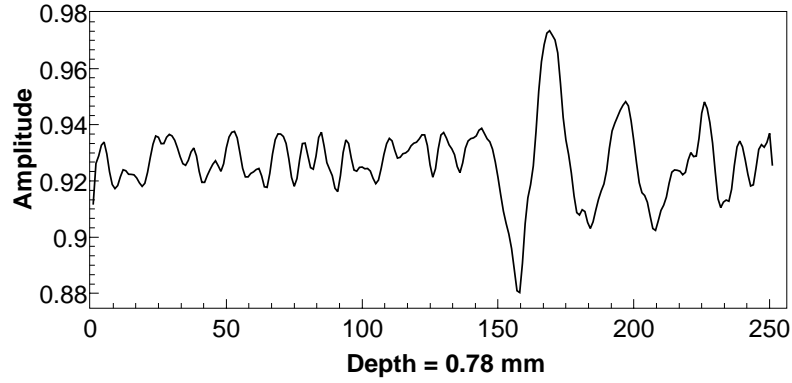
Figure 3.2: A-line signal from a vessel of mouse brain.

3.1.1   Median filtering

The image after bandpass filtering is undergone median filter to remove further impulse noise from the PA image. Median filtering is a non-linear process useful to preserve the information at the edges. In median filtering, neighboring pixels are sorted in an increasing order, according to intensity values and then mid value is assigned to the central pixel. The main advantage of median filtering over Gaussian filtering is that it preserves the edges information which is critical in some applications, whereas Gaussian filtering
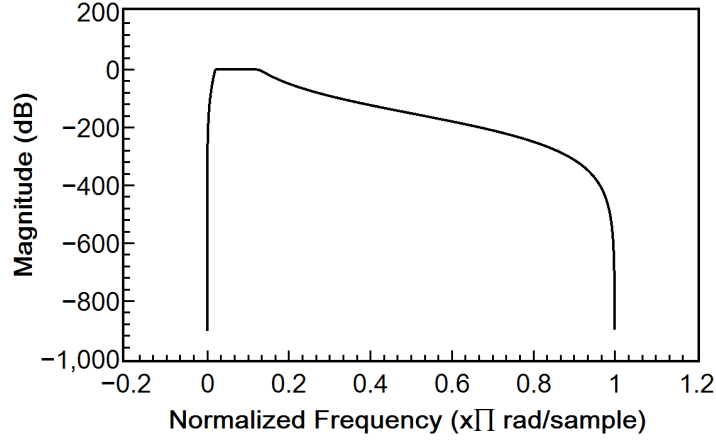
Figure 3.3: Magnitude response of a bandpass filter.
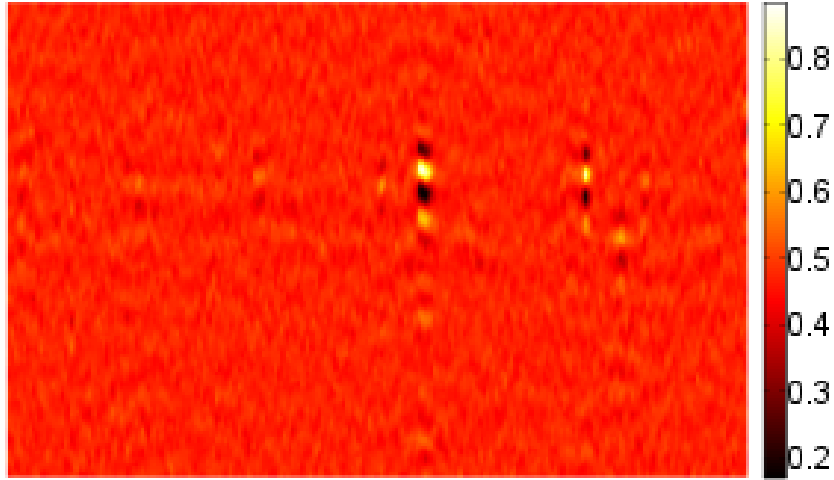
Figure 3.4: B-mode image of mouse ear vessel.

smooths the edges even disappear the small features if big Gaussian kernel is chosen [3]. Several advanced methods of median filtering has also been reported [18, 22, 66, 82]. In the proposed technique an ordinary 3×3×3 median filter is used. The impulsive noise shown in Figs. 3.7 and 3.8 which is re-
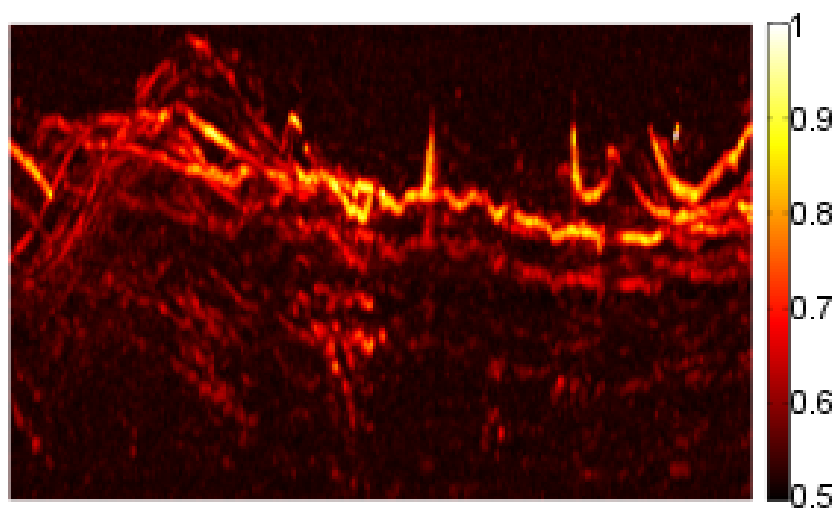
Figure 3.5: Cross sectional view of 3D mouse ear vessels.
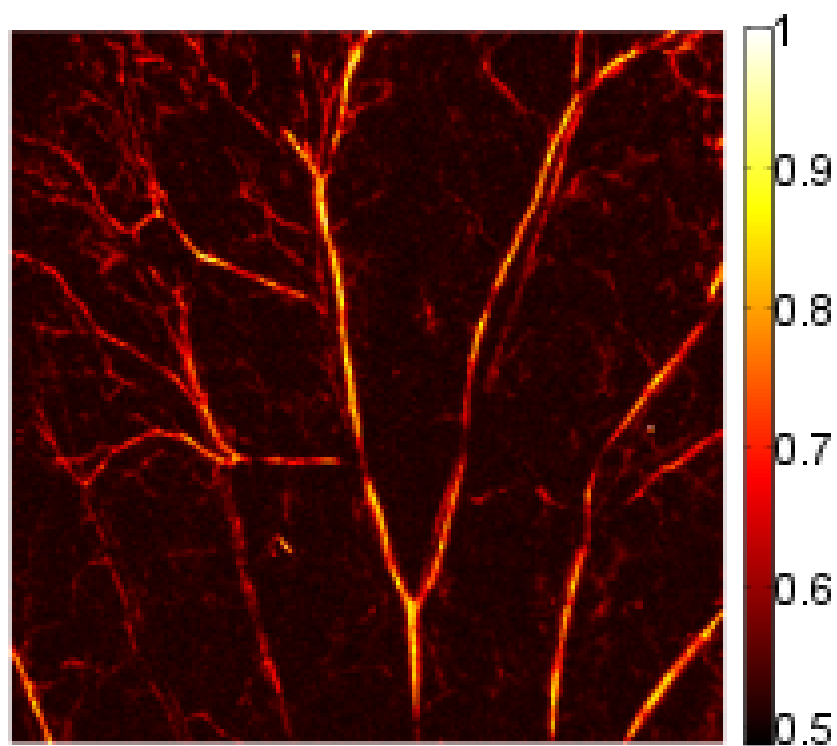
Figure 3.6: MAP image of mouse brain vessels.
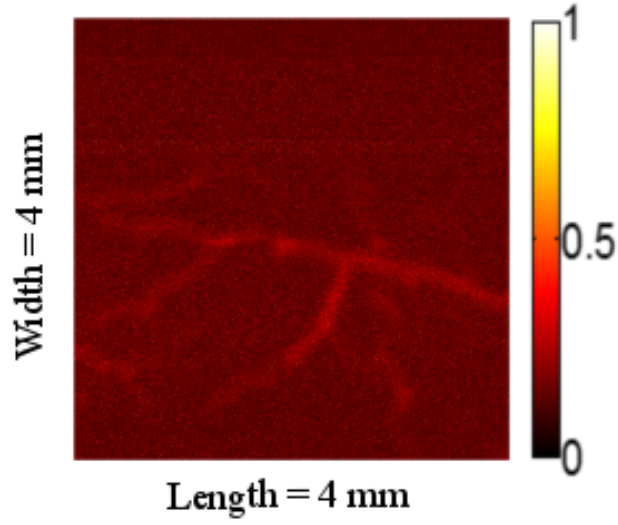
Figure 3.7: Unfiltered MAP image of mouse brain vessels.
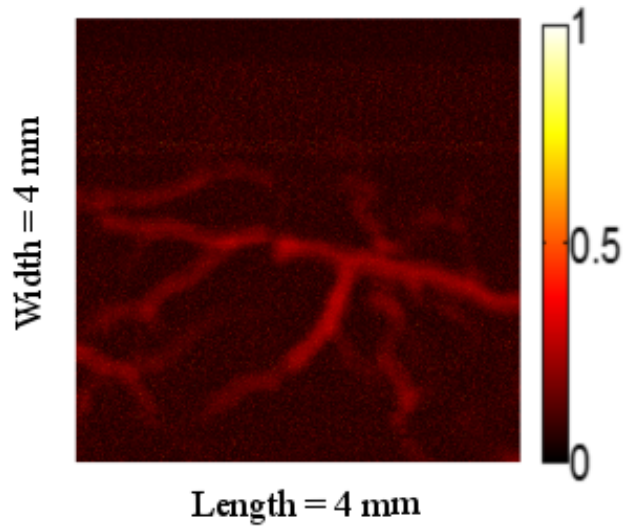
Figure 3.8: Filtered MAP image of mouse brain vessels.

moved by applying median filtering. Fig. 3.9 shows PA image after applying median filtering. Vessels can be easily distinguished from the background after applying median filtering on mouse brain vessels [25, 26, 73].
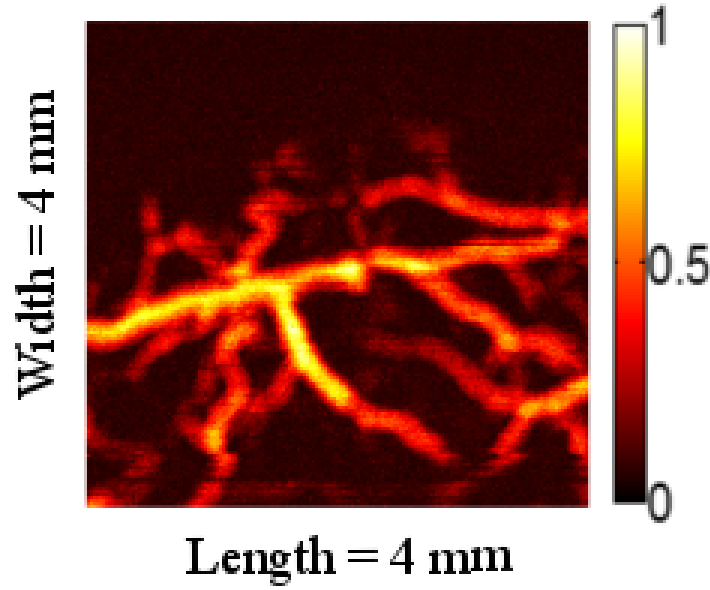
Figure 3.9: Filtered MAP image of mouse brain vessels.

3.2   Summary

In this chapter the pre-processing step to denoise PA images is discussed. In pre-processing the image is first bandpass filtered to remove high and low frequency components. The resultant image after bandpass filtering does not remove the impulsive noise in the PA image, to remove such noise median filtering is applied. The resultant image after applying median filter shows that vessels can be discern from the background but still the image needs further processing for better vessel visualization. In order to do so effect of vessels is further enhanced by Gabor wavelet filtering which is discussed in chapter 5.

Chapter 4

Sparse representation based denoising of PA images

Sparse representation of signals have been widely used for denoising, compression and for making high resolution images. In this chapter spares representation is used for the denoising of PA image. K-means singular value decomposition (K-SVD) is used to update the dictionary. The dictionary is updated at each iteration and image is denoised at each iteration as well. This iterative process minimize the error which is measured by comparing with the reconstructed image until the convergence criteria is met. The results show to be highly effective at denoising PA images. [1]

Introduction

Several methods have been proposed for the reconstruction and denoising of vasculature in PA imaging. The most widely used is Hessian based method proposed by [20] and further explained in [51]. They proposed a multi-scale vessel enhancement method by obtaining the eigenvalues of Hessian matrix, based on these eigenvalues tubular structures were classified in the image. Small and big vessels are enhanced using multi-scale analysis in Hessian based method. At low scale vessels with smaller radii are preserved, whereas at large scale bigger vessels are better preserved. Hessian based method is able to reconstruct vascular networks by removing the background noise and improves the contrast at the expense of smoothing the vessel edges.

[57] proposed a method to enhance the effect of curvilinear structures such as vessels and bronchi in the three-dimensional (3D) images. In their proposed method 3D line enhancement filter was used to distinguish between line and other structures. The line filter is based on a combination of the eigenvalues of the Hessian matrix. [24] used Singular Value Decomposition (SVD) to denoise the photoacoustic images. They used SVD to obtain the sparse representation of the noise and showed the effect of Singular Value Components (SVCs) on the noisy PA images. [75] used contour scanning to increase the signal to noise ratio (SNR) of conventional OR-PAM and claim that it increases the SNR as much as 41% and shortens the image acquisition time by 3.2 times. [42] proposed a combination of model and sparse based method to reconstruct the photoacoustic tomographic images. [54] proposed a method for detecting blood vessels in medical images in which the assump-

tion of cylinder at each voxel in the image is omitted. They extracted the characteristics of local intensity in a spherical polar coordinate system and common properties shared by the polar neighborhood intensity profiles belonging to vascular system were used. They claim that the proposed method improves the vessel detection performance on two-dimensional (2D) and 3D clinical vascular images. [68] presented a shape-tuned strain energy density function to measure the complex vasculature in 3D images which are difficult to measure at bifurcations in Hessian based method because of the oversimplified cylindrical model. Model based reconstruction methods of vasculature have been also widely used to extract vascular structures. The standard method to denoise vasculature in photoacoustic images is based on wiener filter [9, 32]. This method have been widely used for denoising because of its simplicity. However, a crucial assumption in wiener filter is that power spectral densities (PSDs) of noise and signals are known a priori.

On the other hand, sparse representation based denoising has also been widely used for image denoising [12, 17, 31, 44, 55]. K-SVD uses sparse coding as one of its initial step to compute sparse representation for all of its input image patches [36]. One of the main step of K-SVD is dictionary learning and a lot of literature is already available to learn dictionaries. Here we will reference the one used to design K-SVD [1]. The K-SVD method can also be useful in other image processing applications like demosaicing, inpainting and denoising. Here we consider the use of K-SVD to denoise photoacoustic images for vessel reconstruction.

4.1   Materials and Methods

4.1.1   Experimental setup of OR-PAM

In OR-PAM the laser beam is focused by an objective and two prisms separated by a thin layer of silicon oil under the objective and correction lens which is used to align the optical excitation and acoustic detection. The OR-PAM system (Micro Photo Acoustic Inc. in NY ,USA) and (Advanced Optowave Corporation, NY, USA) with laser wavelength of 532 nm, pulse duration 8 ns and pulse repetition frequency (PRF) of 5 kHz was used to irradiate tissues. The ultrasound with center frequency of 20 MHz and sampling rate of 500 Mbps was used to acquire PA image. The maximum lateral and axial resolutions of the system are 5 μm and 15 μm respectively. The maximum imaging depth of the system is 1 mm below this limit the incident light undergo scattering which jumbled up the light path and inhibits effective optical focusing. The image contrast is based on optical absorption, which shows that technique is well suited to visualize blood vessels due to strong optical absorption of hemoglobin. Since, HbR and HbO_2 are two major sources of optical absorption in tissues and PAM is well suited to image blood vessels within the spectral region [38, 62]. Each laser pulse produces one A-Line which is one-dimensional (1D) depth resolved image. The volumetric image is acquired by 2D raster scanning of ultrasonic transducer along the transverse plane [28, 72]. The B-scan rate for a 2-mm line is 5 Hz with 0.625 μm step size. If the ultrasonic detector with high central frequency, large numerical aperture and bandwidth is employed, the PA source can be visualized with high spatial resolution [79].

4.1.2   Image reconstruction

The proposed method for reconstruction and denoising of photoacoustic imaging has several computational steps. The flow diagram of the proposed method to reconstruct vasculature is shown in Fig. 4.1.

In the first step the raw signal is zero centered by subtracting the mean of the data. Then the signal is pre-processed by band pass filter around the center frequency of the transducer. It is important to choose an appropriate pre-processing technique to denoise the image, which varies from application to application. Bandpass filter removes the high and low frequency components in the image which suppresses the noise and increases SNR. Then median filtering is applied to remove impulse noise in the image. The pre-processing step should be selected such that it performs well in terms of denoise with less computation complexity. Denoising using sparse coding requires K-SVD algorithm [36] to update the dictionary. The iterative process of updating the dictionary to minimize the noise requires high computation time. To make the denoising process efficient, images are first down-sampled. The information in 3D PA images can be seen by calculating the Maximum Intensity Projection (MIP) image, which is a 2D projected image of maximum values along the A-lines of 3D volume data. Fig. 4.2 shows the smoothed A-line signal along the depth of data. MAP images hide the detail beneath the vessels. In order to visualize 3D vasculature, all the A-lines or B-mode images need to be denoised. In the denoising process B-Mode images are filtered separately and for the reconstruction of MIP image, all the filtered B-mode images are stacked and maximum intensity along the (A-Line) depth
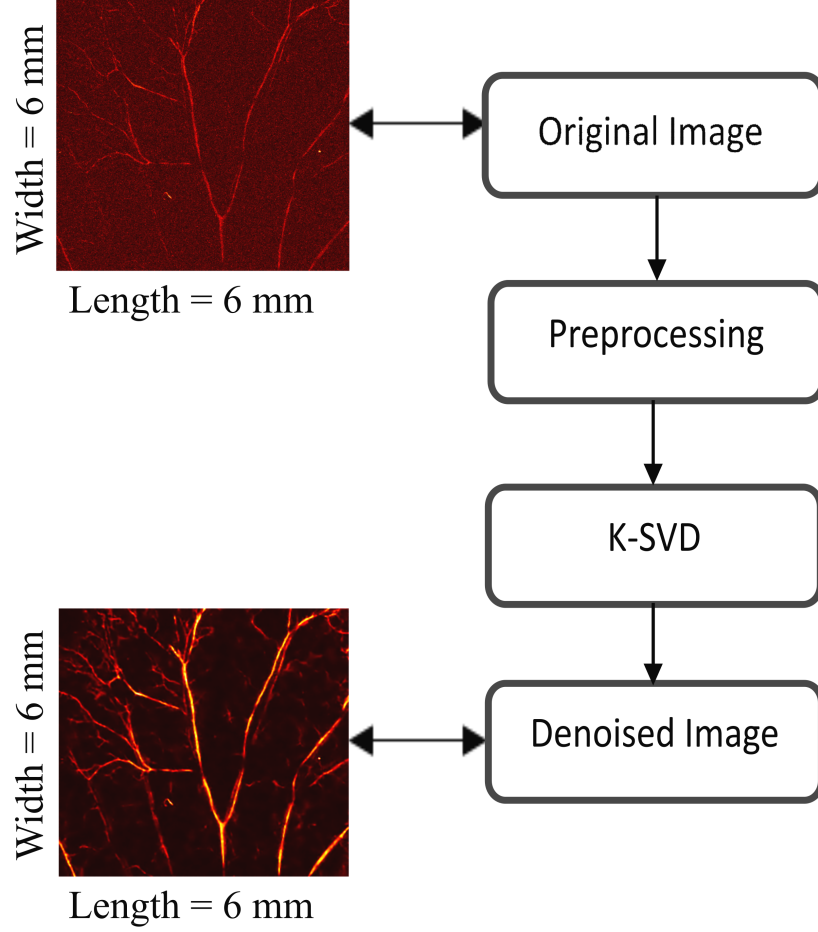
Figure 4.1: Flow diagram of the proposed method.

is taken.

4.1.3   K-SVD based denoising

Sparse coding is a process of computing representation coefficients $\mathbf{x}$ based on the given signal $\mathbf{y}$ [1]. Sparse representation based denoising increases the signal to noise ratio, thus enhancing the vascular structures by decreasing the noise. Recent years have shown a great interest in the research of sparse
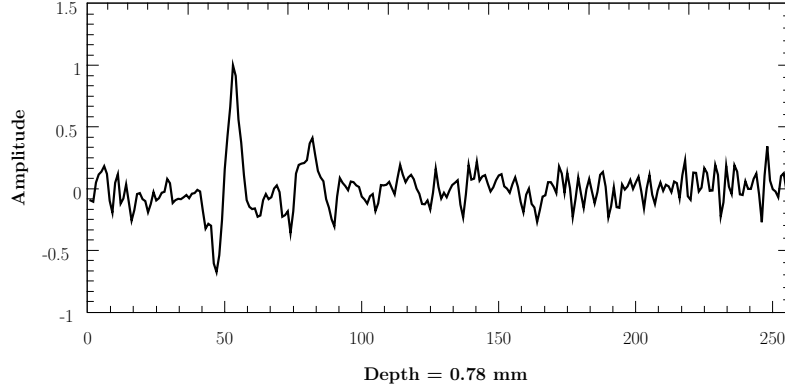
Figure 4.2: A-line signal along the vessel of 3D data.

based signal representation. The problem of image denoising can be solved as, an ideal image $\mathbf{x}$ is recovered in the presence of noisy image $\mathbf{y}$, the algorithm removes noise from the noisy image $\mathbf{y}$ by getting as close to the original image. Measured image $\mathbf{y}$ is given in Eq. 4.1.

$$y = x + a. \tag{4.1}$$

The basic model suggests that signal can be represented efficiently as a linear combination of atoms, where most of the linear coefficients are sparse.

If x is a column signal and $\mathbf{D}$ is the dictionary with columns as atoms, the sparse approximation problem can be described as in Eq. 4.2.

$$\hat{\boldsymbol{a}} = \underset{a}{argmin} \left(\mathbf{D}\boldsymbol{a} - y^2 \right). \tag{4.2}$$

The columns of the dictionary are called atoms. The size of the dictionary depends on the number of atoms in it. Eq. 4.3 shows the input image y of size n×p, dictionary D of size n×k and sparse matrix with size k×p. Where n denotes the size of the patches in the input image and number of atoms in

the dictionary, k and p are the dictionary and sparse matrix size respectively.

$$y_{(n \times p)} = D_{(n \times k)} \mathbf{a}_{(k \times p)}. \tag{4.3}$$

At first, dictionary $\hat{\mathbf{D}}$ is initialized by selecting random patches from the noisy image [36]. In the first step sparse matrix is created from each patch of the noisy image $\mathbf{R}_{ij}\mathbf{y}$. Sparse matrix is built such that it has only a few non-zero coefficients and distance between the $\mathbf{R}_{ij}\mathbf{y}$ and sparse approximation $\hat{\mathbf{D}}\hat{\alpha}_{ij}$ is minimum. In the second step each column of the dictionary $\hat{\mathbf{D}}$ and representation $\hat{\alpha}_{ij}$ is updated such that patches in $\mathbf{y}$ become more efficient, which can be achieved by minimizing Eq. 4.4 using orthogonal matching pursuit. The image is reconstructed iteratively by averaging the patches in each iteration and process is continued until the error is minimized.

$$\sum_{i,j} ||(\hat{\mathbf{D}}\hat{\alpha}_{ij} - \mathbf{R}_{ij}\mathbf{y})||^2. \tag{4.4}$$

To denoise the image, k iterations are performed to minimize the error. Each patch $\mathbf{R}_{ij}\mathbf{y}$ corresponds to the denoised version of the image. Finally, all the patches are stacked to reconstruct the final version of denoised image.

In the first step a fixed dictionary $\hat{\mathbf{D}}$ and sparse representation $\hat{\alpha}$ of the image patches are computed. Different methods have been proposed for the calculation of sparse vector typically it is done by finding the approximate solution using any pursuit algorithm. The simplest are matching pursuit (MP), orthogonal matching pursuit (OMP) and order recursive matching pursuit (ORMP) [11,67]. These are greedy algorithms and simple to imple-

ment, which is just the calculation of inner products of signals and dictionary atoms [55]. In our calculation we used OMP, this method selects the dictionary element with maximum projection on to the signal residual assuming the dictionary atoms are normalized. The main steps for finding the sparse solution of a given noisy image y and dictionary D are described below

Task: Given a noisy image y, approximate the solution such that

$$\min_x ||\mathrm{x}|| \quad \text{s.t.} \quad ||y - Dx||_0. \tag{4.5}$$

To update the dictionary K-SVD algorithm is used which is effective method of training dictionary. It starts with an initial dictionary D_0 and improves the dictionary iteratively to achieve the sparse representation of the signals in y. The steps to update the dictionary are described below

Parameters: A randomly generated dictionary **D**, signal **y** and the threshold ϵ.

Initialization: Start from the iteration $k = 0$, initialize the sparse vector $x = 0$ and residual $r = y - Dx$.

Iteration: Increment k by 1 while performing the following steps.

1. Select the element with maximum correlation with the residual by using Eq. 4.6.

$$\mathrm{i} = argmax|d_i^T r|. \tag{4.6}$$

Compute the error $E = \min_x ||\mathrm{Dx\text{-}r}||_2^2$.

2. To update the dictionary, each column $l = 1,2,...,k$ in D is updated by finding the set of patches that use the atom l.

3. For each column of the dictionary its representation error is calculated as shown in Eq. 4.7

$$\mathbf{e}_{ij} = \mathbf{R}_{ij}X_{ij} - \sum_{m \neq l}\mathbf{D}\alpha_{ij}, \tag{4.7}$$

   where m is the selected atom.

4. Set E_l as a matrix whose columns are e_{ij}.

5. Apply SVD, $E = U\Delta V^T$ choose the updated column of dictionary to be the first column of U and coefficient values to be the values of V multiplied by $\Delta(1,1)$.

OMP is used iteratively to obtain near optimal set of representation vectors. The steps to find the sparse matrix using OMP are described below.

1. The initial solution $x^0 = 0$.

2. The initial residual $r^0 = b - Ax^0$.

3. Find the index ψ_t by solving the Eq. 4.8

$$\psi_t = argmax <\mid r_{t-1}, \phi_j \mid>, \tag{4.8}$$

   where ψ_t is the indices location where there is maximum inner product between the residual r and measurement matrix ϕ.

4. Solve the least-square problem to obtain the signal estimate: $x_t = argmin_x||\phi_t x - v||_2$.

5. Calculate the new approximation and new residual. $a_t = \phi_t x_t$

   $r_t = v - a_t$.

6. Increment t and repeat from step 3 until convergence.

The final image is reconstructed by averaging over the patches Eq. 4.9.

$$X = [\lambda I + \sum_{ij} R_{ij}^T R_{ij}]^{-1}[\lambda Y + \sum_{ij} R_{ij}^T D\alpha_{ij}]. \tag{4.9}$$

Where I is the identity matrix and λ is the weighting parameter of identity matrix. The inverted matrix is diagonal and the value of a pixel in the denoised image is calculated by averaging the value of this pixel in the noisy image weighted by λ. Once this is done, a new averaging is calculated over all the image patches.

4.2 Experiments and results

Experimental subjects

In this section the experimental subjects to test the method is discussed. The algorithm is tested on two subjects for its validation.

1. Blood filled tube.

2. Mouse ear vessels.

These cases were considered in order to reconstruct the vasculature in the noisy photoacoustic images. The experiments performed on animals in our study were approved by Ethical Committee Review Board of Tohoku University. For laser safety, standards defined by American National Standards Institute (ANSI) Z136 are followed. The algorithm was implemented on MATLAB (2015) and ImageJ was used for the visualization of 3D data [59].

4.2.1   Blood filled tube

In the first experiment 3D photoacoustic images of blood filled tubes of diameter 100, 200 , 300, 400 and 500 µm were tested. The acquired size of the data was $256{\times}400{\times}400$, where 256 data points show the depth of A-lines, $400{\times}400$ data points are the length and width of the data respectively. The length and width of $8\,mm{\times}8\,mm$ is divided into $400{\times}400$ data points. The diameters measured from reconstructed images were closed to the actual diameters of the tubes. Original MIP and reconstructed images are shown in Fig. 4.3. Length and width of the photoacoustic image are $8\,mm{\times}8\,mm$ in the x and y plane respectively, z being the depth along A-line. One-dimensional profile taken along the length is shown in Fig. 4.4. One-dimensional profile shows the noisy and filtered tubes. The black holes in the tubes or low intensity values show the low concentration of blood in that area, where as the high amplitude shows high concentration of hemoglobin in the blood.
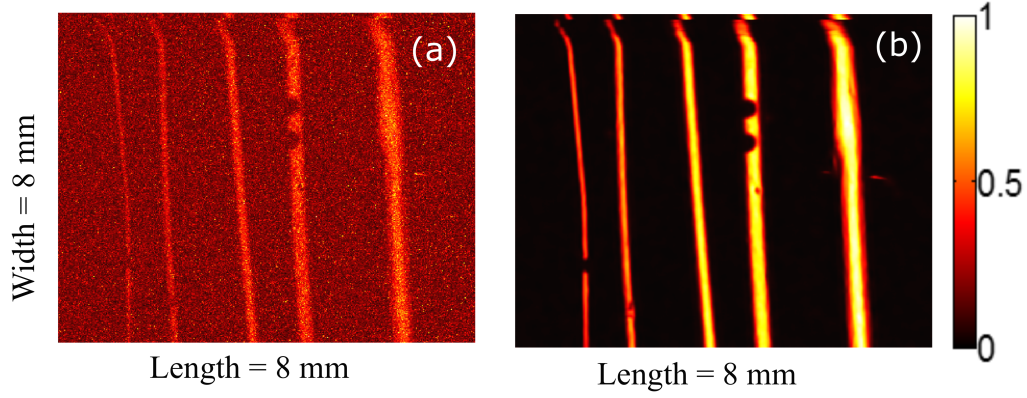
Figure 4.3: a) Raw image maximum intensity projection; b) Denoised MIP image of blood filled tubes.

4.2.2 Mouse ear vessels

This section describes the results of reconstructed vasculature of mouse ear. Mouse having weight of 28.5 g and length of about 10 cm. Mouse ear was scanned with laser having wavelength of 532 nm. The filtered image shows the clear distinction between the background and the vasculature. The 3D acquired data was 0.78 mm×6 mm×6 mm, which are depth, width and length respectively. The total time to acquired 3D data was 18 minutes and the time to acquired 1 B-mode slice was 2.7 seconds. Fig. 4.5 (a) shows the original 2D image of mouse ear vessels. Fig. 4.5 (b) shows the denoised MIP image of mouse ear.

4.3 Discussion

In this work, the problem of denoising of PA images is considered where the level of noise is not known a priori. K-SVD algorithm depends on the
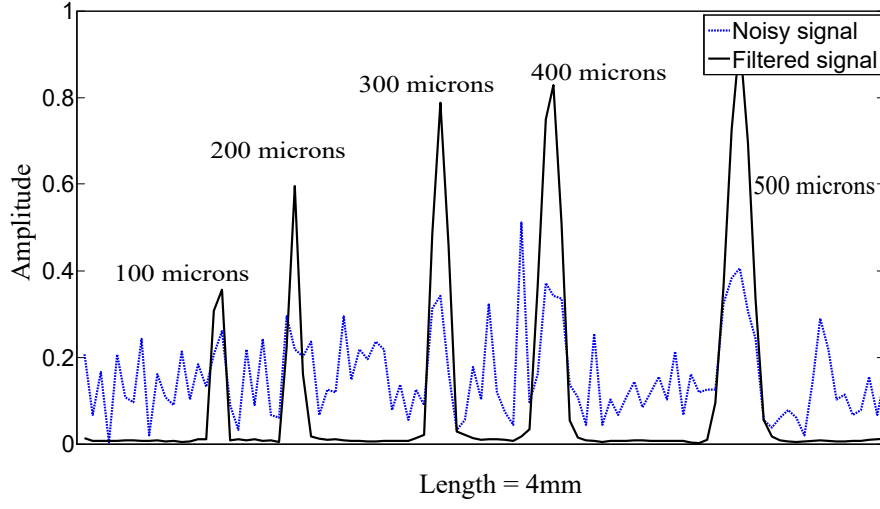
Figure 4.4: One dimensional profile of blood filled tubes.
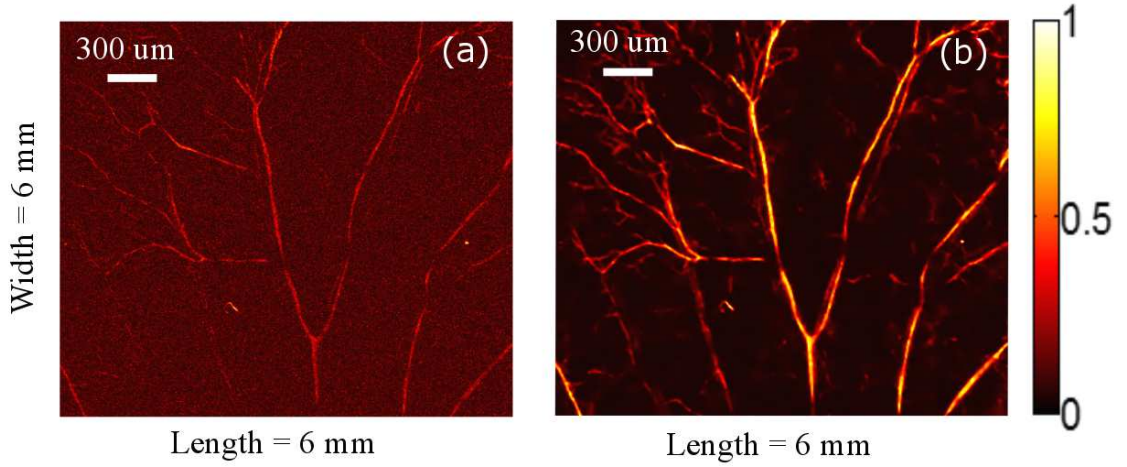
Figure 4.5: (a) Noisy image; (b) Denoise image with KSVD.

selection of parameters and number of iterations to denoise the image. The 3D dataset is first bandpass filtered and smoothed with 3×3 median filter and then the algorithm is applied on each B-mode of 3D dataset. In order to acquire an image of high resolution, a dataset with more data points are needed, which increases the computation time and requires number of
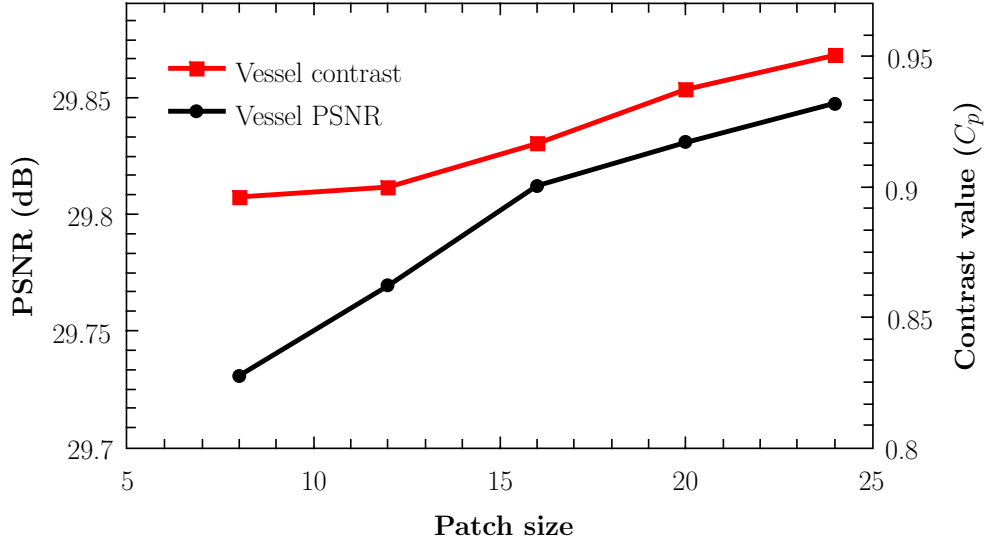
Figure 4.6: Graph between the PSNR and patch size.

iterations to denoise each B-Mode image. Down sampling the original data loses the information but decreases the computation time as well. Denoising of only MIP image gives better result at the cost of hiding small vessels under the big vessels. Two quality measures were considered to validate the performance of K-SVD for PA imaging, i) Peak Signal to Noise Ratio (PSNR) and ii) Contrast between vessels and background (C_p). At first stage, size of the patch is defined in K-SVD. Effect of different patch sizes 8, 12, 16, 20 and 24 against PSNR is shown in Fig. 4.6. The second quality measure, the calculation of contrast between vessels and background is defined as:

$$C_p = \left| \frac{V - B}{V + B} \right|, \tag{4.10}$$

where V and B are average gray values of the vessels and background respectively. The larger value of C_p indicates more obvious difference between blood vessels and the background. Fig. 4.6 shows the effect of vessel

contrast and PSNR with increasing patch sizes. The patch size 8x8 gives low contrast and PSNR because the vessel properties are not covered by the patch. Increase in the patch size increases the PSNR and C_p, shows that bigger patch size covers the global properties of vessels. To investigate the effect of white noise on PA images and noise removing capability of K-SVD, different noise levels ($\sigma = 7, 9, 11, 13, 15, 17$) were introduced in the image. The mouse ear image is first reconstructed with optimal parameters (discussed in 4.3.1) and then different noise levels were added in the image [74]. Fig. 4.7 shows the quality performance of K-SVD over standard wiener and wavelet filtering. In wavelet filtering soft thresholding is used to increase the PSNR and optimal threshold is chosen where the PSNR is maximum. Increasing in Gaussian noise reduce the PSNR of original signal. At low Gaussian noise a little difference is observed in the PSNR of K-SVD, wiener and wavelet filtering. Difference in the PSNR increases as the noise level increases, which shows the better denoising capability of K-SVD over wiener and wavelet based filters.

4.3.1   Parameter selection

Several parameters were considered for the denoising of PA images; dictionary atoms, patch size of the input image and Gaussian kernel size for multiscale vessel denoising.
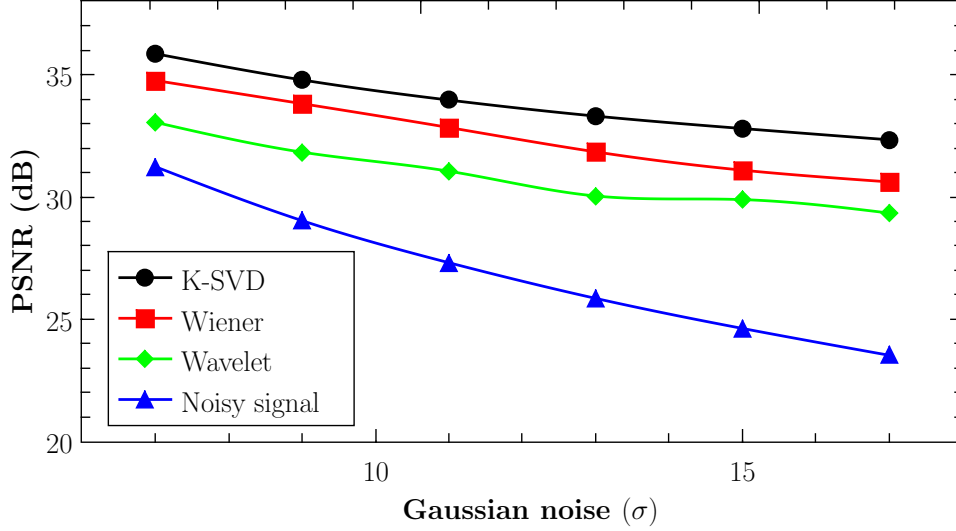
Figure 4.7: Comparison of K-SVD with Wiener and wavelet based denoising.

Dictionary size

Pre-selection of the dictionary size is important as it effects the output qual-
ity of the image. Dictionary with small number of atoms decreases the com-
putation time but also deceases the denoising capability of the algorithm,
on the other hand increasing the size of dictionary atoms increases the com-
putation time but also increases the denoising capability of the algorithm.
In our case where the primary focus is to denoise blood vessels in 3D PA
volumetric data, size of the dictionary is chosen such that it increases the
output image quality of blood vessels. The dictionary is trained on the noisy
patches and updated using KSVD algorithm. Fig. 4.8 shows the increase of
PSNR with the increase in size of dictionary atoms. Figs. 4.9 and 4.10 show
the dictionaries learned on noisy image patches. Small patches are 8×8 in
both dictionaries.
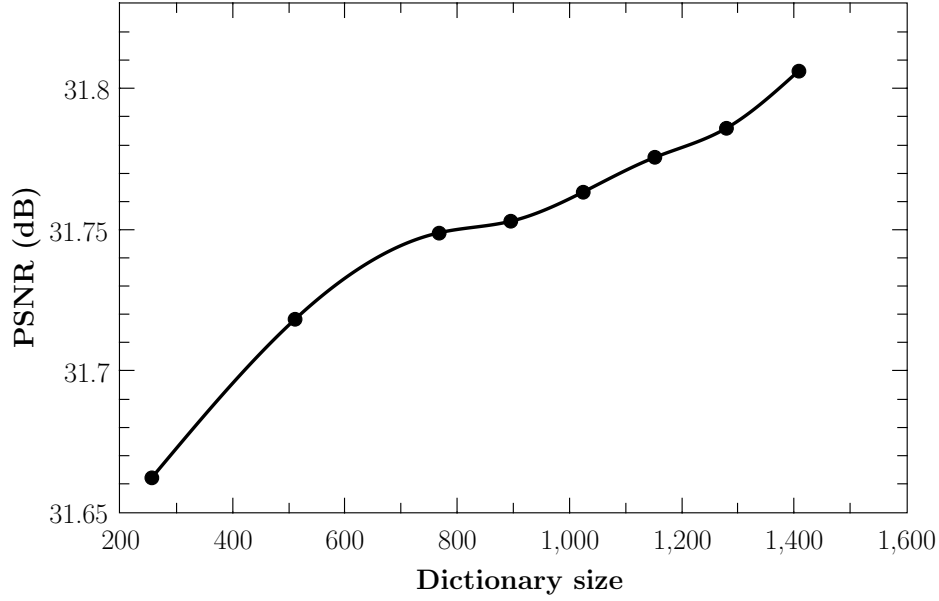
Figure 4.8: Graph between the PSNR and dictionary size.

Patch size

Patch size also effects the output image quality. Selecting small patch size only denoise the vessels where the diameter is in the range of the patch. To denoise the image, patch size is selected such that global properties of the vessels are covered in the patch. Increasing the patch size increases the computation time and PSNR of the image.

Gaussian kernel size

The size of the Gaussian kernel depends on the noise in the image. Selecting small Gaussian kernel increases the computation time but also increases the PSNR of the output image. Increasing the size of the Gaussian kernel denoise the image at the cost of smoothing the blood vessels and disappearing small vessels. In case of photoacoustic images we know the property of the noise
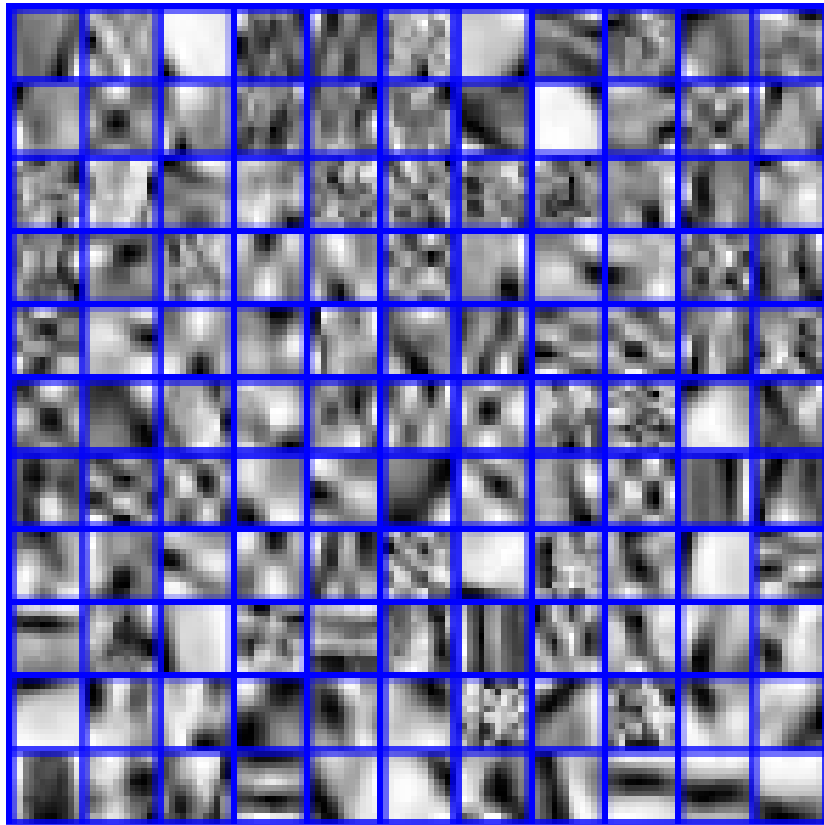
Figure 4.9: Dictionary trained on noisy image having dictionary atoms = 88.
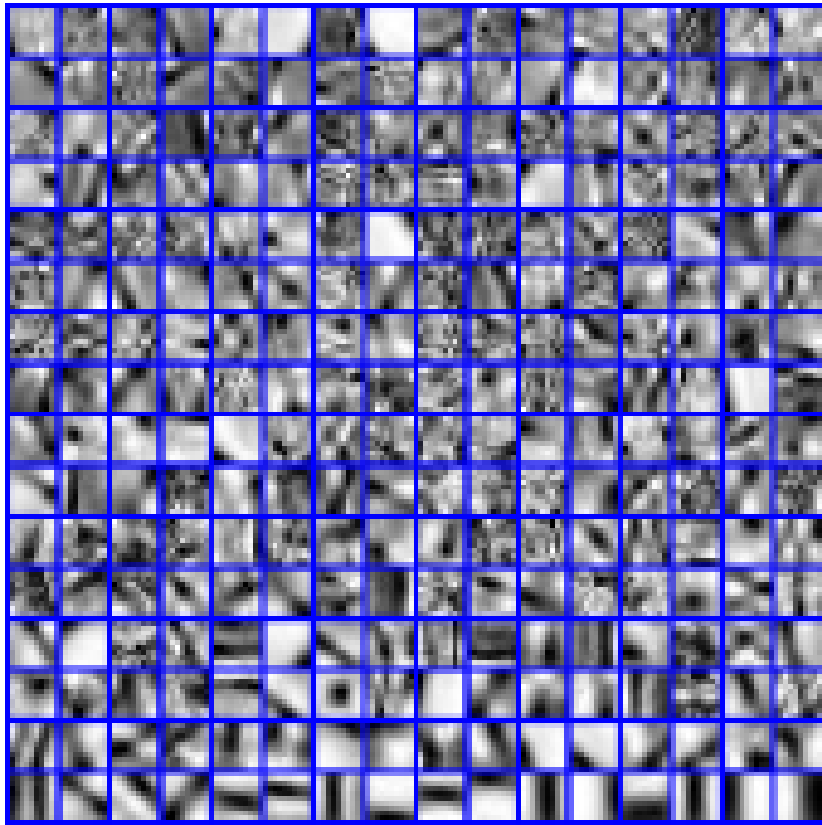
Figure 4.10: Dictionary trained on noisy image having dictionary atoms = 256.

from number of images acquired from OR-PAM, based on this we can tune optimal parameters for better quality and less computation time.

The selection of the parameters varies from application to application. The following parameter values were chosen in order to denoise photoacoustic images with PSNR more than 35.89 (dB). Patch size = 8×8, Number of dictionary atoms = 64, Gaussian kernel standard deviation = 8.

The limitation of the OR-PAM system used in our study has a maximum penetration depth of 1 mm. Blood vessels within the range of 1 mm can be seen but small vessels deeper than this depth can be made visible but still difficult to visualize.

4.4   Summary

In this chapter, a K-SVD method for denoising of PA images is presented. The denoising process uses the sparse decomposition of blocks of noisy image and adaptive dictionary which is trained on noisy image to denoise the output photoacoutic images. which performs better in terms of output image quality to denoise photoacoustic images. The algorithm has a high computation time to perform on all slices of 3D volume data. The algorithm can be used to denoise PA images, but still there are small vessels which are difficult discern from the background. There is need to improve the algorithm to enhance the effect of small vessels in the image. The method has better denoising capability as compared to standard methods for denoising. Moreover, this method can be integrated with model based reconstruction to enhance the image quality. The k-SVD method offers room for improvement

towards other imaging modalities as well.

Chapter 5

Vascular structure enhancement

In this chapter a method to enhance the effect of vasculature from background using 3D Gabor wavelet filtering is proposed. The 3D directional Gabor wavelet filtering is used to enhance the effect of vessels in each direction, since the vessels in 3D volumetric data may exist in every direction. To enhance the effect of vessels of different radii, size of the wavelet is changed within a specific range by changing its parameters is also discussed in this chapter. The validity of this method to enhance the effect of vasculature is shown by applying the proposed method on PA images acquired from OR-PAM. The enhanced vasculature images are further processed by Hessian based filtering which is discussed in this chapter. [1].

---

[1] The proposed method in this chapter is published as a part in

5.1   Introduction

Wavelet filtering have been widely used to process medical images. Wavelets can easily be presented as mathematical formulae, and can be understood in terms of correlation with the signal being analyzed. Frequency components in time signals with constant frequencies can be visualized by taking ordinary Fast Fourier Transform (FFT) of the signal. However, sometimes the frequency of the signal changes at different interval of time. Such signals can easily be handled with wavelets because of their ability to deal with time and frequency simultaneously. Wavelet is a waveform of limited duration, irregular and can be non-symmetric signal. The anomalies and other information in the signal can better be described by wavelet.

Wavelet transforms are multiresolution decomposition and can be used for images as well. They can describe the signal at different scale and position to visualize the useful information while suppressing the noise. In many medical applications noise can be minimized by taking averaging over many signal acquisitions which leads to trade off between imaging time and signal-to-noise ratio (SNR). [10, 14, 69]. In this research diameter of the vessels are enhanced by choosing the appropriate standard deviation of the Gaussian function. A range of standard deviation is defined in order to enhance the effect of vessels. This range is defined manually.

5.1.1   Gabor wavelet

Gabor function was proposed by Dennis Gabor in 1946 [21]. Nowadays, Gabor functions are widely used for feature extraction, edge enhancement, classification and segmentation. In images, different features can be visualized with the help of wavelet transform. Gabor wavelets are created from one atom and by changing the parameters like dilation, elongation, orientation and frequency of the atom complete image representation can be obtained [37,37,45]. In case of two dimensional Gabor function, it is correlated with the image to enhance the effect of specific features in image, it provides the information of local spectral energy density concentrated at a given position and frequency at specific direction. Vascular structure in retinal images can be extracted using 2D Gabor wavelet. Fig. 5.1 shows the vessel enhancement at different angles in 2D retinal image. Fig. 5.2 shows the combine effect of 2D Gabor wavelet.

In case of 3D Gabor filter it is considered as ellipsoid with side lobes and direction. In this research work we introduced a 3D Gabor wavelet to enhance the effect of vessels in different direction in OR-PAM images. A complex Gabor filter can be defined as the product of a Gaussian kernel and complex sinusoid. Eq. 5.1 shows the 2D Gabor wavelet function.

$$g(x, y, \lambda, \theta, \psi, \sigma, \gamma) = exp\big(\frac{x'2 + \gamma^2 y'2}{2\sigma^2}\big) exp\big(i\big(2\pi\frac{x'}{\lambda} + \psi\big)\big) \qquad (5.1)$$

In eq. 5.1, θ represents the orientation λ represents the wavelength, ψ represents the phase offset, γ is the spatial aspect ratio and σ is the standard deviation of the Gaussian function. The equation can be written in other
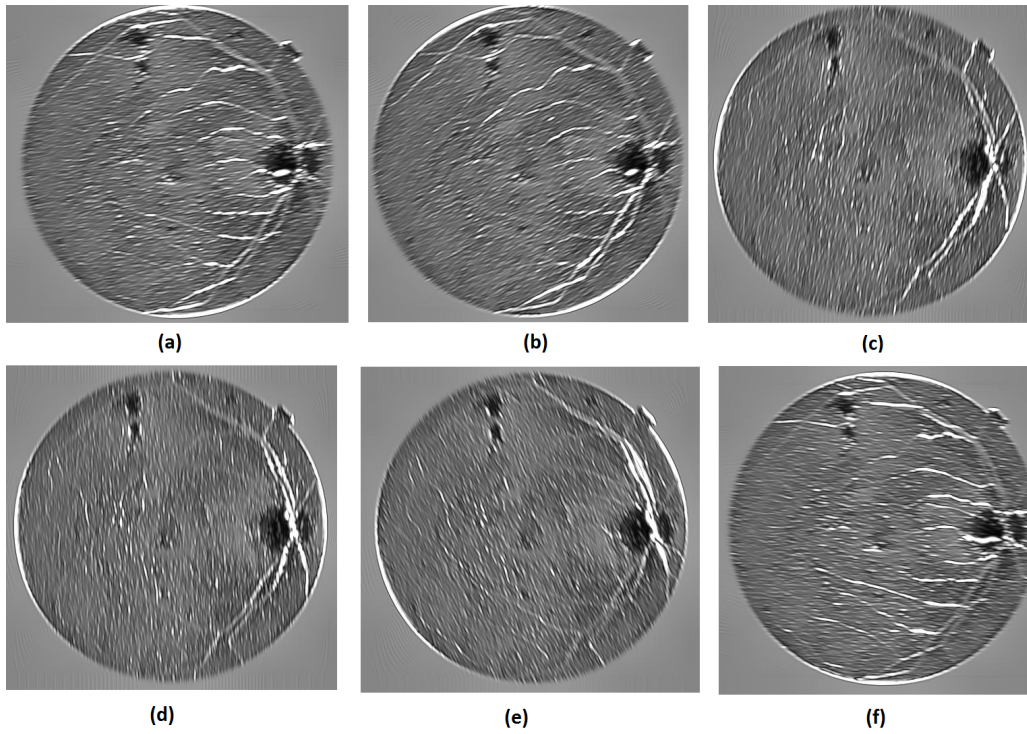
Figure 5.1: Vessel enhancement at different angles in retinal image.
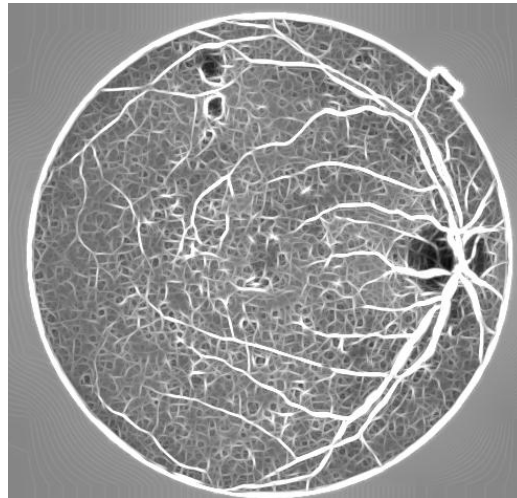
Figure 5.2: Gabor wavelet filtering.
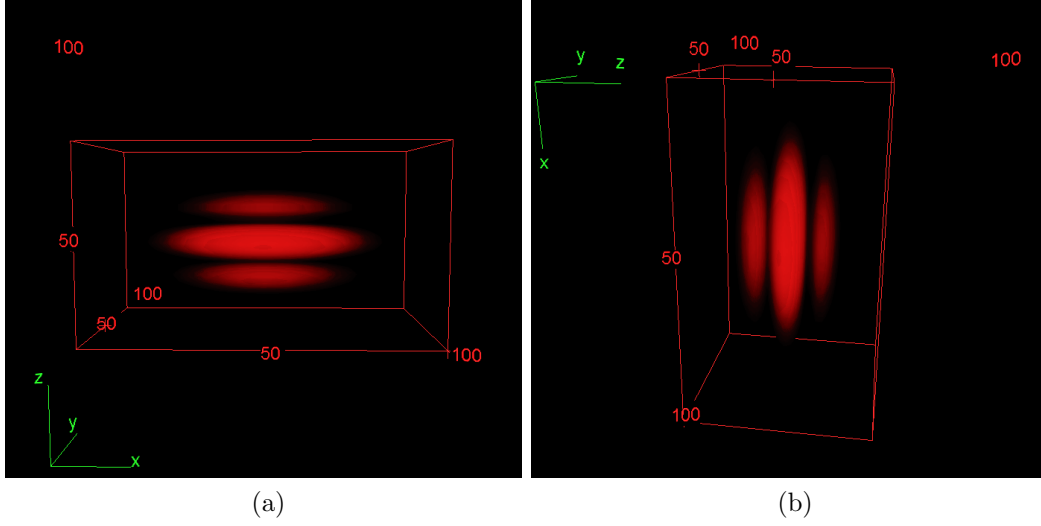
Figure 5.3: (a) Gabor wavelet at 0°; (b) Gabor wavelet at 90°.

form for 3D as

$$\psi_M(x) = exp(jk_0.x)exp(-\frac{1}{2}|Ax|^2) \tag{5.2}$$

where $j = \sqrt{-1}$, $A = diag[\epsilon^{-\frac{1}{2}}, 1]$ and the frequency of the complex exponential is controlled by the vector k_0, $\epsilon \geq 1$ that defines the elongation in particular direction.

These parameters are used to create different wavelets for filtering, based on these parameters features in the image can easily be enhanced. 3D Gabor wavelet at two different angles are shown in Fig. 5.3.

3D Gabor filtering is useful to enhance the effect of vessels in 3D space. Applying 2D Gabor filter on slices of 3D volumetric data loses the continuity of in images, if there exist vascular structures the continuity of vessels can be lost. In order to maintain the continuity of 3D vasculature 3D Gabor wavelet shown in Fig. 5.3 at different angles is used. To control the direction,

orientation and frequency of the wavelet parameters shown in Table. 5.1 are adjusted depending on the smaller, bigger and direction of the wavelet. As discussed in chapter 3 bandpass filtered image is enhanced by Gabor wavelet. Fig.5.4 shows the enhanced vascular structure by applying Gabor filtering. The steps to enahnce 3D PA volumetric data are described below.

1. Gabor wavelet of different standard deviation is rotated from $\theta°$ to $180°$ and correlated with the median filtered image.

2. The 3D Gabor wavelet is correlated with raw 3D volumetric data in any two orientations from x, y and z respectively.

3. Response at each angle is preserved.

4. Maximum of the response from all the angles give the enhanced vascular image.

5. Repeat step 1 to step 4 for different dilation parameter of Gabor wavelet.

Table 5.1: Gabor wavelet parameters.

Parameters	Values
Angle (θ)	10°
Dilation (α)	6
Elongation (ϵ)	3
Frequency (K_0)	[0 0 1]

Selection of parameters vary from application to application, in case of vessel enhancement a range of vessel radii is pre-defined to enhance the effect
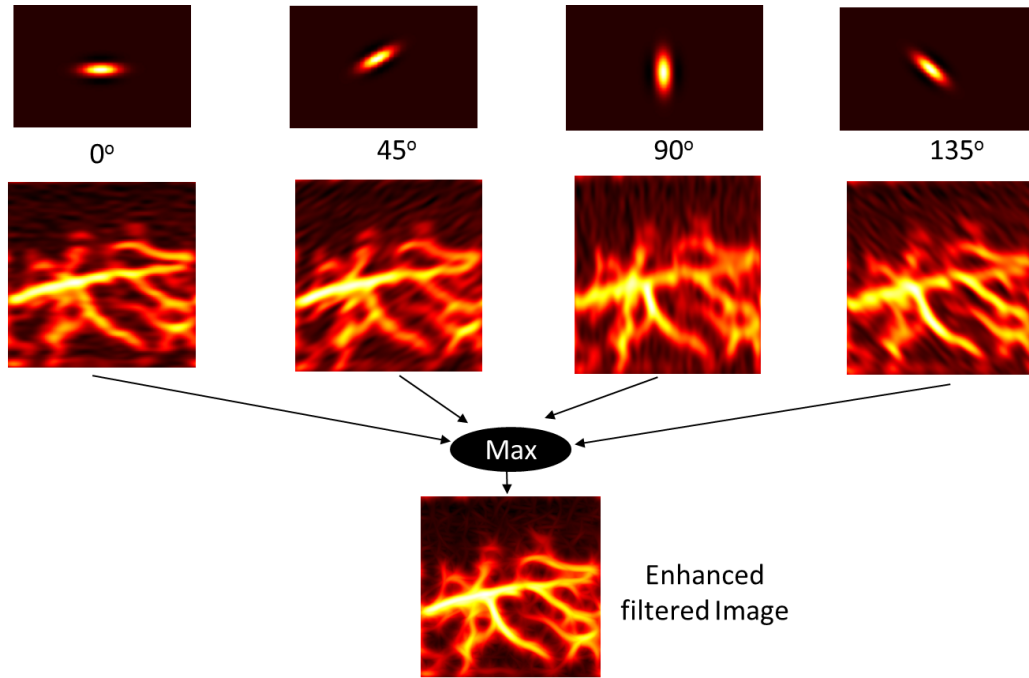
Figure 5.4: Enhanced vascular structure of retinal image by Gabor wavelet filtering.

of vessel in that particular range. The shape of the Gabor wavelet has a main lobe and side lobe centered at zero. The width of the main lobe is chosen such that it enhances the effect of vessel having the same diameter as the width of the main lobe.

5.1.2   Effect of scaling

Scaling of Gabor wavelet is important to enhance the effect of smaller and bigger vessels. Bigger vessels are easy to visualize and distinguishable from the background, whereas small vessels are difficult to discern from the background; starting from a small scaling value and increasing with an increment enhances most of the vessels. Fig. 5.5 shows the effect of scaling at different

<div align="center">(a)   (b)   (c)</div>
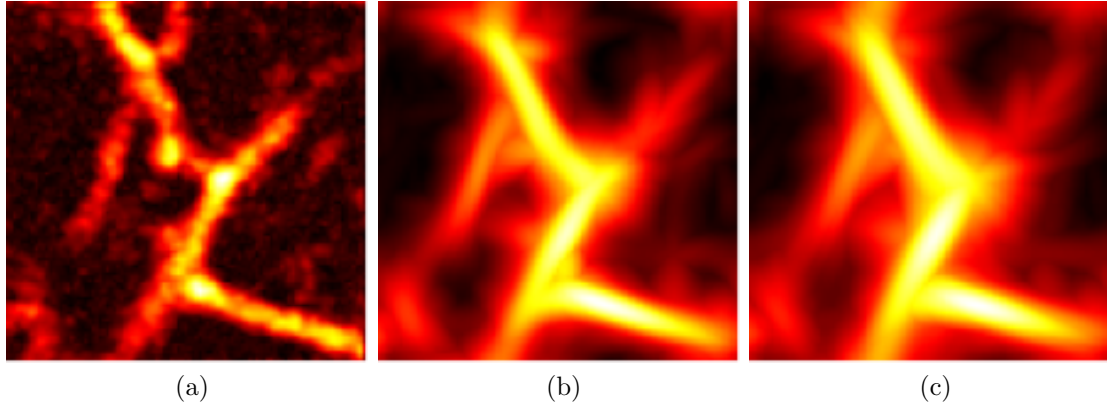
Figure 5.5: Effect of varying scaling of Gabor wavelet on vascular structure.
(a) Dilation value = 1; (b) Dilation value = 3; (c) Dilation = 4.

values.

5.1.3   Effect of Elongation

Elongation is useful to enhance the directivity of the vessels. Bigger value
of elongation elongate the vessel in that particular direction. Value of elon-
gation is chosen wisely and vary from application to application choosing
too big value will prolong the vascular effect even at bifurcation and at end
points. Fig. 5.6 shows the effect of elongation at different values.

5.1.4   Effect of Frequency

Frequency parameter of Gabor wavelet is set after checking the response by
varying the frequency. Fig. reffrequency shows the effect of different fre-
quencies. Fig. 5.7c shows the effect of higher frequency, where only high
frequency components are visible. So this parameter can be tuned to visu-
alize smaller and bigger vessels, since bigger vessels contain low frequency
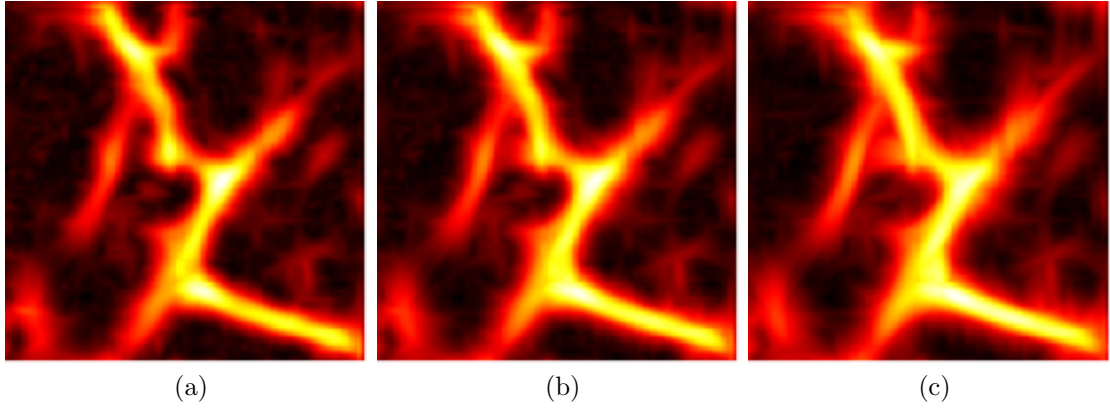
Figure 5.6: Effect of varying elongation of Gabor wavelet on vascular structure. (a) Elongation = 10; (b) Elongation = 20; (c) Elongation = 40.
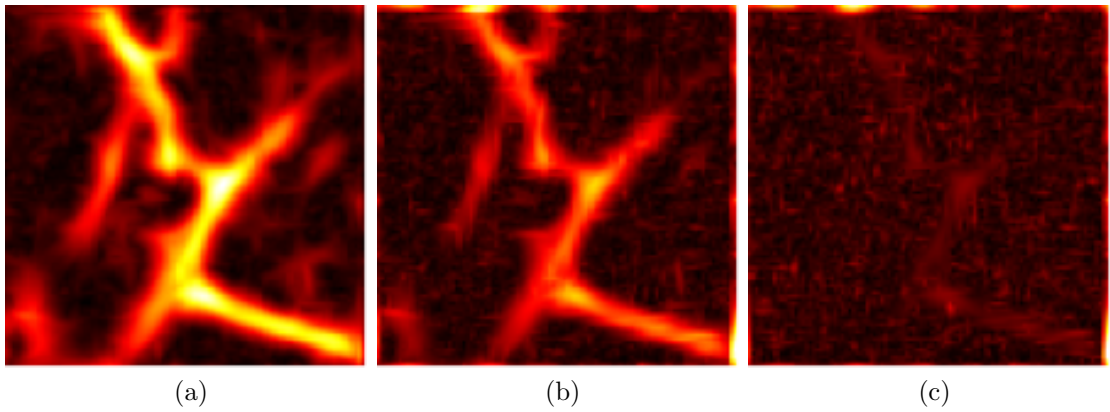
Figure 5.7: Effect of varying frequency of Gabor wavelet on vascular structure. (a) Frequency = 1; (b) Frequency = 2; (c) Frequency = 2.5.

components and small vessels contain high frequency components.

The enhanced vascular image is further processed with Hessian based filtering to enhance the effect of curvilinear structures and to suppress the noise. The output image of Gabor filter is the enhanced image of all the vessels in the PA image.

5.2   Hessian based filtering

Several methods have been proposed to enhance curvilinear structures [20, 30, 56, 57]. In this research work we detect the curvilinear structures by Hessian based method which mainly depends on eigenvalues of the Hessian matrix. The basic aim of using this method is to discriminate between line like and other structures. The multi-scale Hessian based method provides significantly improved visualization of curvilinear structures. The detailed analysis of Hessian method is discussed here. In human body various types of curvilinear structures like blood vessels, bronchial trees and other tube like structures exist. There has been a considerable research work done on the enhancement and extraction of vessel like structures from 3D images. The images acquired from MRI, CT, PET and other imaging modalities, these imaging modalities give the information of vascular structures but still the image quality is insufficient for vessel visualization. In OR-PAM vascular structures can be acquired but the noisy PA images make these structures difficult to visualize. To enhance vessels of different radii multiscale Gaussian kernel shown in Eq. 5.3 is applied to extract vascular structures.

$$G(\mathbf{x}, \delta) = \frac{1}{(\sqrt{2\pi\delta})^D} exp\big(\frac{||\mathbf{x}||^2}{2\delta^2}\big), \qquad (5.3)$$

where $\mathbf{x} = \{x, y, z\}$ is the position in 3D space and δ is the scale used to increase or decrease the standard deviation of the Gaussian function. The 3D image is first smoothed with the Gaussian kernel 5.3, the smoothed image

is computed as

$$I(\mathbf{x}, \delta) = I(\mathbf{x}) * G(\mathbf{x}, \delta), \qquad (5.4)$$

where $I(\mathbf{x}, \delta)$ is smoothed 3D image at scale δ. Local features in the 3D image are found by forming a $3{\times}3$ Hessian matrix at each voxel of the image. The Hessian matrix contains second order partial derivatives which gives the information of local curvatures. The Hessian matrix at position $\mathbf{x}$ is given as

$$H_{(\mathbf{x},s)} = \begin{bmatrix} l_{xx}(\mathbf{x}, \delta) & I_{xy}(\mathbf{x}, \delta) & l_{xz}(\mathbf{x}, \delta) \\ l_{yx}(\mathbf{x}, \delta) & l_{yy}(\mathbf{x}, \delta) & l_{yz}(\mathbf{x}, \delta) \\ l_{zx}(\mathbf{x}, \delta) & l_{zy}(\mathbf{x}, \delta) & l_{zz}(\mathbf{x}, \delta) \end{bmatrix}, \qquad (5.5)$$

where lxx is th second order partial derivative with respect to x position, lxy is the second order partial derivative with respect to x and y position respectively and so on. Eigenvalue decomposition of $3{\times}3$ Hessian matrix gives three eigenvectors at each voxel point, the eigenvectors represent a new orthonormal coordinate system which represents the local curvature. The corresponding eigenvalues define the magnitude of these vectors and gives the information of the curvature in the direction of eigenvectors. Thus these eigenvalues can be used to identify the vasculature in 3D images. The obtained eigenvalues from Hessain matrix are arranged in increasing order $\lambda_1 \leq \lambda_2 \leq \lambda_3$. To identify the curvature a criteria of of eigenvalues is met, where two eigenvalues are higher than the third one. The steps to extract vasculature from 3D image are shown in Fig. 5.8.
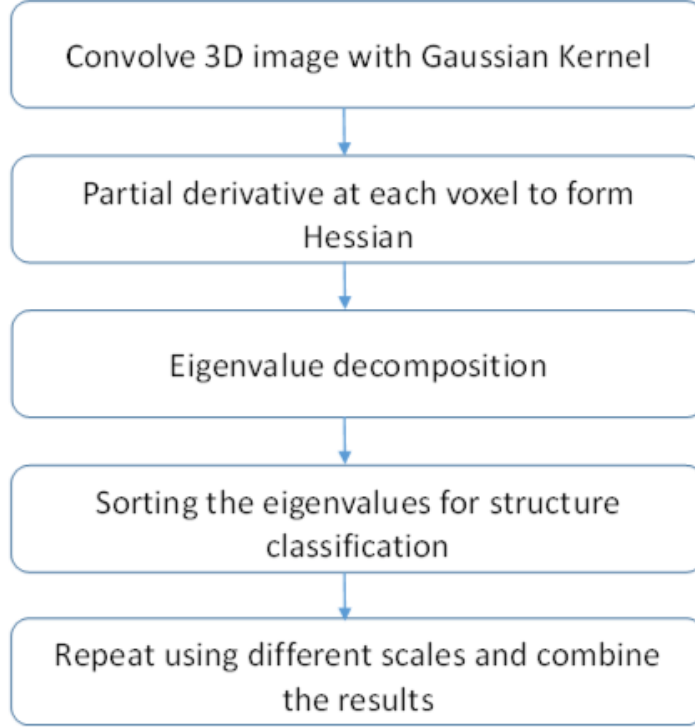
Figure 5.8: Vessel enhancement by Hessian method.

To identify different structures in 3D images, different ratios are defined. The ratio defined in Eq. 5.6 differentiates between vessel and plate like structures.

$$R_A = \frac{|\lambda_2|}{|\lambda_3|}, \tag{5.6}$$

In case of vessel like structures two larger eigenvectors cross through the vessel cross section and the third eigen vector in the direction of the vessel is small. In case of plate like structure one eigenvalue is larger than other two eigenvalues. The maximum value is 1 in case of vessel like structure and 0 for plate like structures.

The ratio in Eq. 5.7 differentiates between blob and plate like structures

$$R_B = \frac{|\lambda_1|}{\sqrt{|\lambda_2||\lambda_3|}}, \tag{5.7}$$

In case of blob like structures all the eigenvalues are approximately equal in magnitude as blob like structures have high curvature in all directions. Thus these structures can be distinguished by comparing the smallest eigenvalue to the two largest eigenvalues. This ratio attains value of 1 in case of blob like structure and 0 for other structures.

Eq. 5.8 shows the Euclidean norm, to control the signal-to-noise ratio (SNR), this term emphasis the areas of high contrast.

$$S = \sqrt{\lambda_1^2 + \lambda_2^2 + \lambda_3^2}. \tag{5.8}$$

The final equation is formed by combining all ratios. This equation helps to visualize tubular structures while eliminating noise and other structures.

$$y(x, s) = \begin{cases} 0, & \lambda_2^2 > 0 \text{ or } \lambda_3^2 > 0 \\ \left(1 - e^{\left(-\frac{R_A^2}{2\alpha^2}\right)}\right) e^{\left(-\frac{R_b^2}{2\beta^2}\right)} \left(1 - e^{\left(-\frac{S^2}{2\gamma^2}\right)}\right) \text{ else,} \end{cases} \tag{5.9}$$

5.2.1 Effect of tuning parameters

To get better output vascular image, Hessian parameters α, β and γ are tuned.
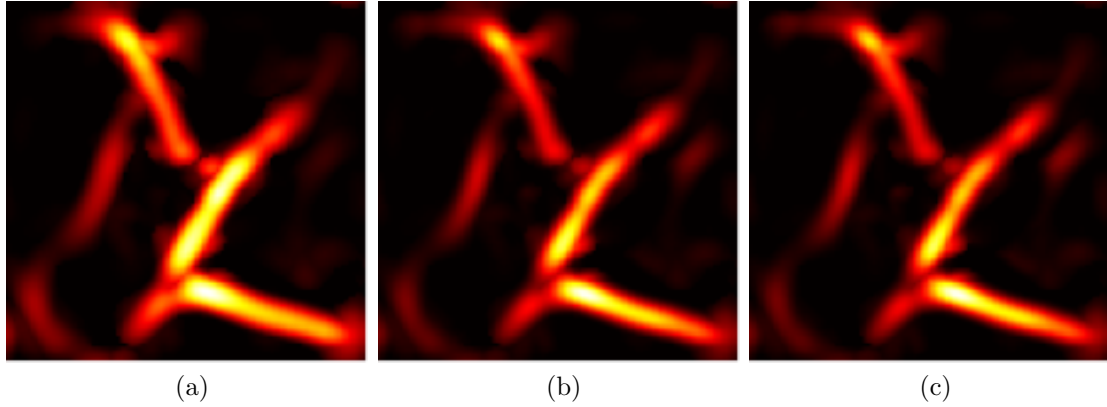
Figure 5.9: (a) $\alpha = 0.1$; (b) $\alpha = 0.5$; (c) $\alpha = 0.9$.

Effect of tuning parameter α

To control the sensitivity of vessel and plate like structures α is adjusted accordingly. Fig. 5.9 show the effect of this parameter on the output image. A slight difference in intensity and vessel radii is observed by changing the value from 0.1 to 0.9.

Effect of tuning parameter β

This parameter controls the sensitivity between blob and plate like structures. Fig. 5.10 shows the effect of different values of β. At smaller value of β blob like structures stand out. as shown in Fig. 5.10a, whereas large value of β enhances the vascular effect in an image shown in Figs. 5.10b and 5.10c.

Effect of tuning parameter γ

This parameter controls the sensitivity of SNR and helps to visualize tubular structures in 3D images. Fig. 5.11 shows the effect of γ on vascular image.
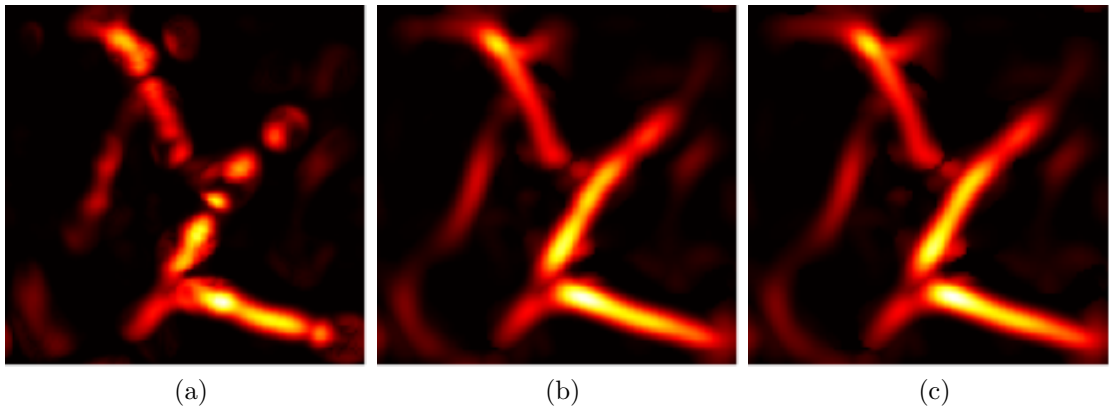
Figure 5.10: (a) $\beta = 0.1$; (b) $\beta = 0.5$; (c) $\beta = 0.9$.
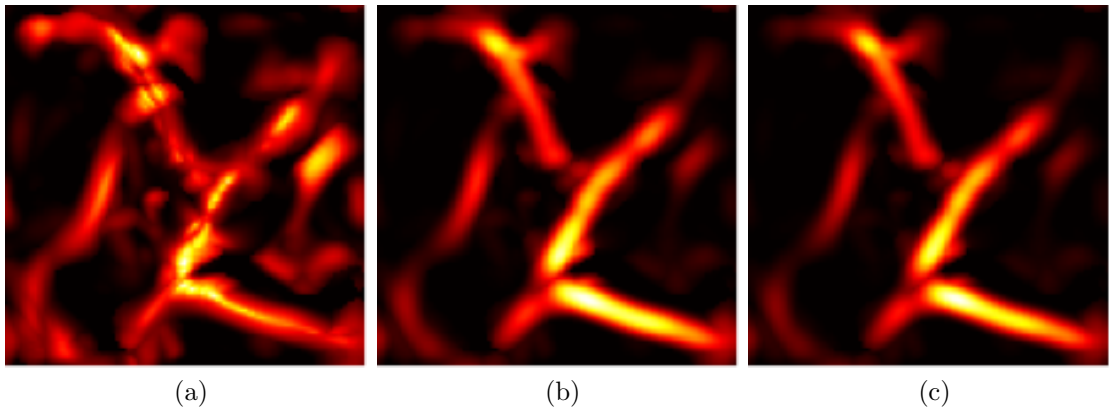
Figure 5.11: (a) $\gamma = 0.1$; (b) $\gamma = 0.5$; (c) $\gamma = 0.9$.

Small value of γ as shown in Fig. 5.11a where tubular structures are not clear but as the value of γ increases tubular structures become more prominent and vessels with high contrast remained in the image.

5.3 Integrated method of Gaussian and Hessian based filtering

The two methods Gabor wavelet filtering and Hessian based method discussed in sections 5.1.1 and 5.2 have limitations. The Gabor wavelet method being the directional vessel enhancement filter also induces the blurriness in the image. The Hessian base method uses the Gaussian function to enhance the effect of vessels. The integrated method of combining these methods overcome the limitations in these methods individually. The result of applying this method on mouse brain vessels is shown in Fig. 5.12. The results of vasculature in human finger cuticle by the proposed method is shown in Fig. 5.14. Fig. 5.13 shows the human finger cuticle. The width and length; scanning area is shown in black dotted rectangle and black tape is used as a reference point that is starting point of scanning. Fig. 5.14a shows the MAP image of human finger cuticle. The noise in the image makes these vessels difficult to distinguish from background. Fig. 5.14b shows the reconstructed image using Hessian based method. The vessels by applying only Hessian based method lacks the directionality due to which continuity in the vessels is difficult to maintain. Fig. 5.14c shows the combined effect of Gabor wavelet filtering and Hessian based method. Applying Gabor wavelet filtering before Hessian method enhances the directionality and maintains the continuity of vessels in 3D images. Fig. 5.14d shows the one-dimensional profile along the length of vessels. The effect of vessels after applying wavelet and Hessian based method is shown in red, while the one-dimensional profile of Hessian and noisy signal is shown in dotted blue and black line respectively. Fig 5.15
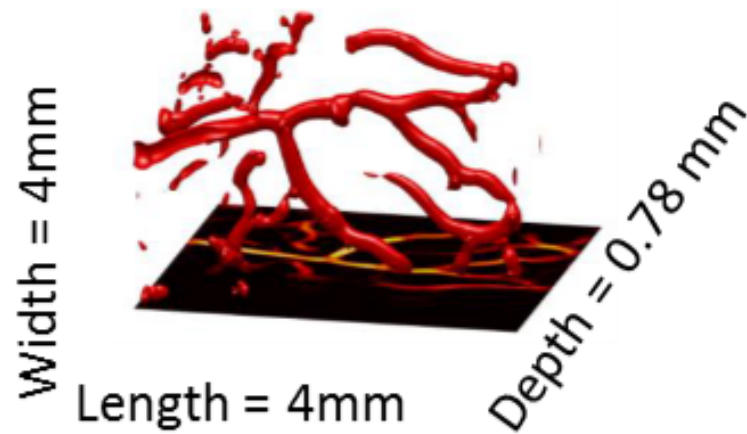
Figure 5.12: Reconstructed mouse brain vessels.

Figure 5.13: Human finger cuticle.

also shows the vasculature in human finger cuticle. Fig. 5.16 shows the 3D vasculature in human finger cuticle.

5.4   Summary

In this chapter Gabor wavelet and Hessian based method for vessel enhancement is discussed. Gabor wavelet is used to enhance the directionality of 3D vascular structures by rotating the wavelet in each direction with some step size. The enhanced vascular image is further reconstructed by Hessian based method. The limitations of both these methods are overcomed by integrating Gabor wavelet and Hessian based method. Effect of different parameters of Gabor wavelet and Hessian based method are also discussed in this chapter. Chapter 4 describes another denoising method to reconstruct vascular structures.
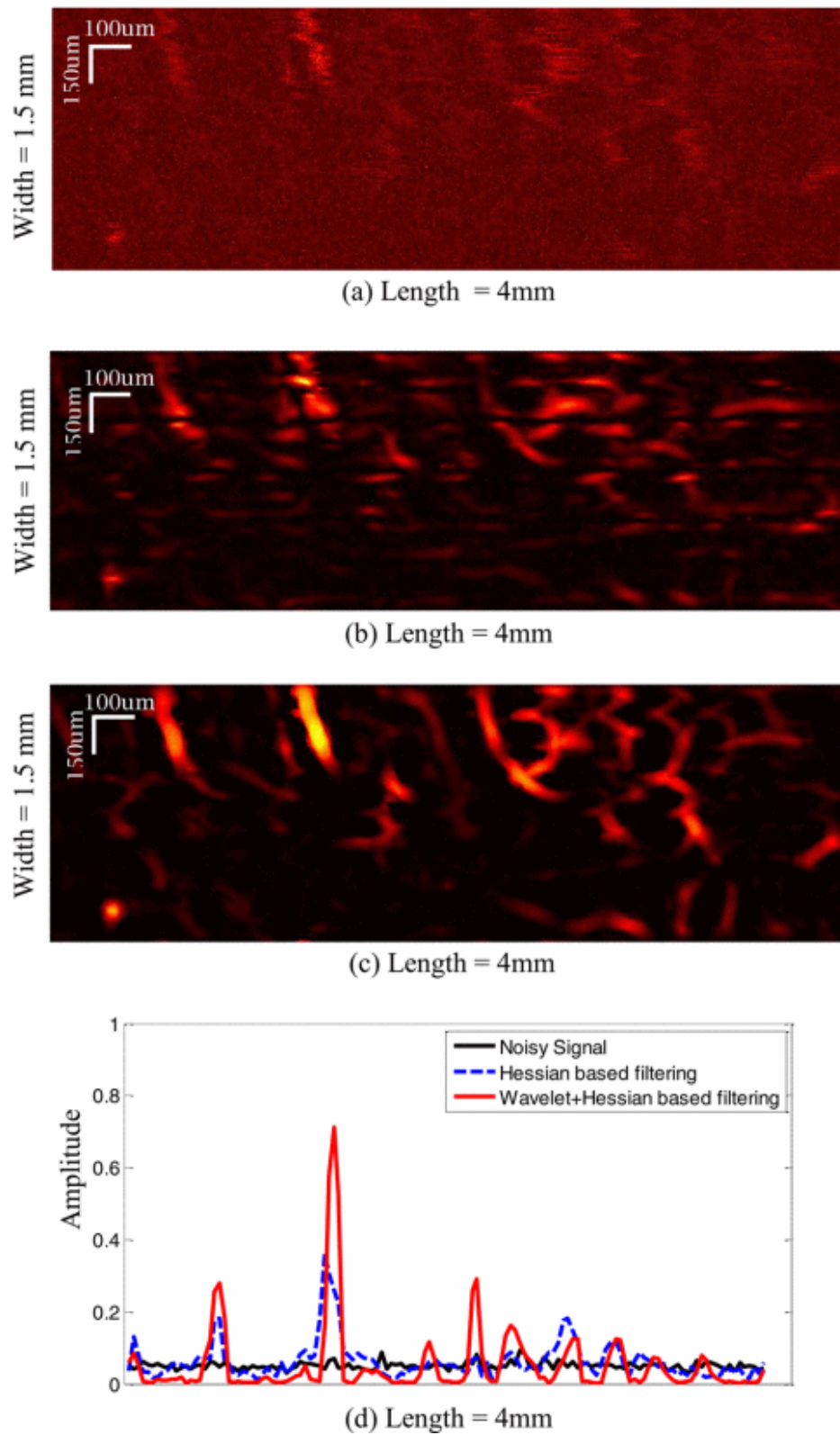
Figure 5.14: (a) Original MIP image of human finger cuticle; (b) Reconstructed MIP image of vasculature using Hessian vessel filtering; (c) Reconstructed MIP image of vasculature using with wavelet and Hessian vessel filtering; (d) One-dimensional profiles of the original and filtered images.

(a) Length = 1.65 mm

(b) Length = 1.65mm

(c) Length = 1.65 mm
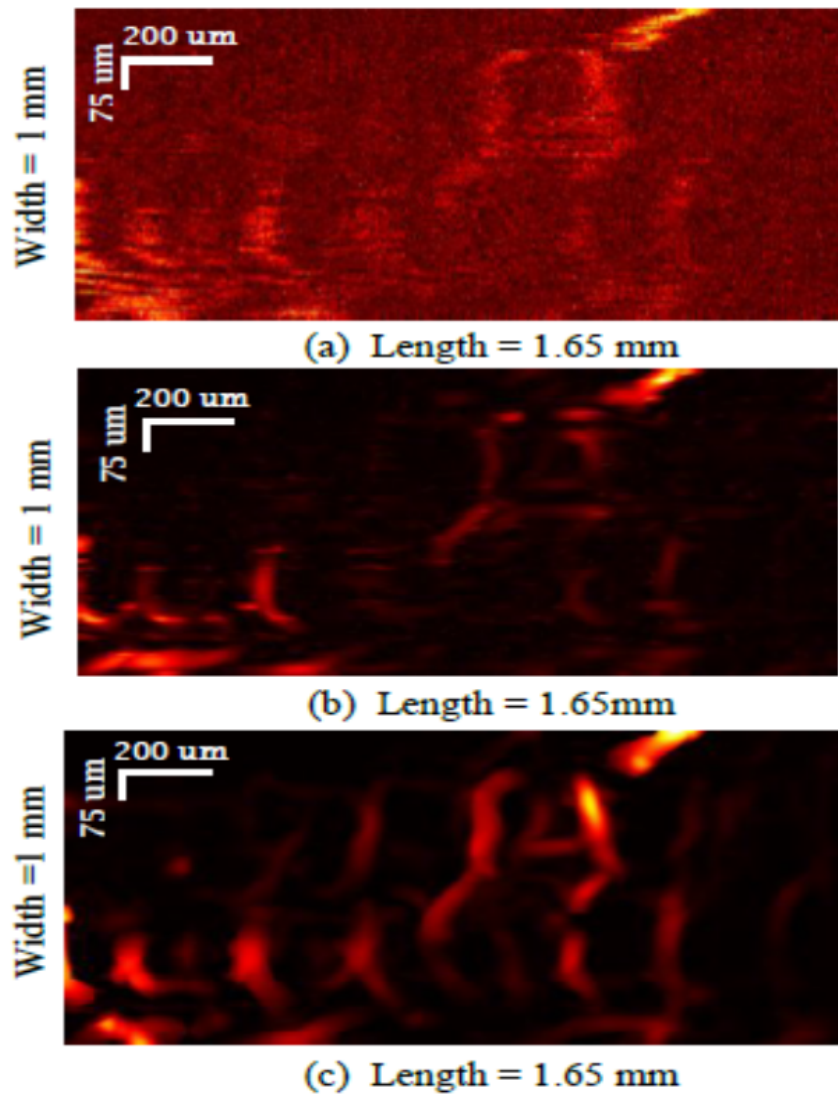
Figure 5.15: (a) Original MIP image of human finger cuticle; (b) Reconstructed MIP image of vasculature using Hessian based vessel filtering; (c) Reconstructed MIP image of vasculature using with wavelet and Hessian filtering.
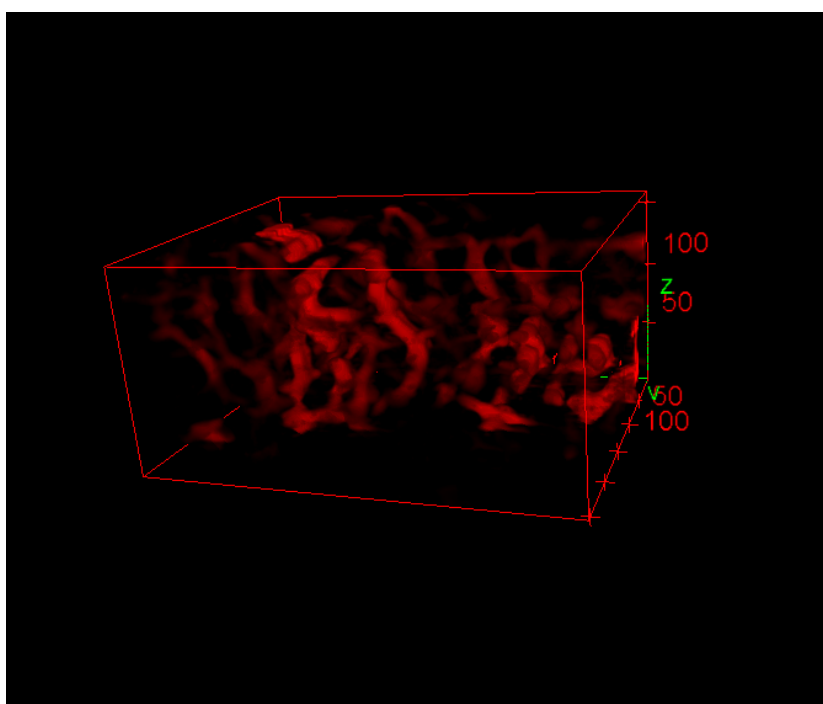
Figure 5.16: 3D visualization of vasculature in human finger cuticle.

Chapter 6

Bifurcation detection by symmetric analysis of eigenvalues

Reconstruction of vasculature in medical images is critical for the early diagnosis of various vascular diseases. In this paper a common method of Hessian based filtering is used to enhance the vascular structures but a different method is proposed to extract the bifurcation (branch) points in 3D photoacoustic images. Bifurcation points play an important role for diagnosis of vessel stenosis, atherosclerosis and surgical planning. In order to clearly visualize the vascular structures, detection of branch points are needed, to enhance the effect of vessels at these points. In the proposed method, first the vascular structure is extracted by eigenvalues analysis of Hessian matrix. Based on the eigenvalues, we detect

73

the bifurcation points by considering a small patch in the image. To detect the branch point, it was analyzed that if the vascular image is rotated from 0° to 180° angles with a small step size θ°, the branch points maintain their rotation symmetry. The algorithm is tested on synthetic data and also on photoacoustic images acquired from Optical Resolution Photoacoustic Microscopy (OR-PAM). The proposed method is shown to be highly effective at detecting branch points. [1]

6.1   Introduction

Medical imaging encompasses many different imaging modalities, It plays an important role to image the human body for diagnostic and treatment purposes. Common imaging modalities include Computed Tomography (CT), Magnetic Resonance Imaging (MRI), Positron Emission Tomography (PET), Ultrasound and X-ray. In this paper we used the photoacoustic images acquired by OR-PAM. It is an emerging imaging technology, that uses the nanosecond laser pulses in the visible and near infrared range to irradiate the tissues, the tissues absorb the laser pulses which results in the excitation of the hemoglobin molecules, this excitation results in the conversion of optical energy into heat energy, which results in the thermal expansion of the tissues and acoustic signal is generated. The generated acoustic signal

---

[1]This chapter has been accepted as

is detected by the ultrasonic transducer. Such imaging modalities are useful to extract vascular structures non-invasive. From the past two decades a significant progress has been made for vessel segmentation and reconstruction, but automatic segmentation of bifurcation points remains a difficult task. One of the most common diseases is atherosclerosis [13], which is the hardening and narrowing of arteries, where the plaque accumulates in the arteries and put the blood flow on risk, which is a usual cause of heart attack. The plaque often happens at bifurcation points, thus in vascular images the visualization and detection of bifurcation is extremely important. In this research we detect the bifurcation points on the synthetic data and also on the three-dimension (3D) volumetric data acquired from OR-PAM.

6.2   Related research

In literature several methods have been proposed to detect branch points. Active models [2,40] and center-line extraction [5,63] for vessel filtering have low response at bifurcation points. Kumar *et al.*, [35] extracted the vascular structure using vessel cross-section area, the method uses the analysis of Hessian matrix. Schneider *et al.*, [61] proposed a 3-D vessel segmentation and center-line extraction based on multivariate Hough voting and oblique random forests. Azzopardi *et al.*, [6] proposed a vascular bifurcation detection method in a segmented retinal images by using combination of shifted filter responses. They calculated the response of their filter by the weighted geometric mean of Gabor filters. Kerneki *et al.*, [33] proposed a method for bifurcation detection which is based on multiscale Hessian analysis, and use

histogram of eigenvectors weighted by the vesselness measure. They claim that pixels with three peaks in their immediate neighborhood are considered as bifurcation candidates. McIntosh *et al.*, [49] proposed a vessel crawl based algorithm that crawls along the vessel to segment and exploring the bifurcation points. Zhou *et al.*, [83] proposed a method to detect the tubular structures based on eigenvalues analysis and for bifurcation detection they used adaptive boosting algorithm. Most of the proposed methods are based on Hessian based vessel filtering which use eigenvalues of the hessian matrix to classify vascular structures [19].

In this paper, the proposed method first extracts the vascular structure using Hessian based method and then eigenvalues of the hessian matrix are used to detect the bifurcation points by checking the rotation symmetry using our proposed formula.

The rest of the paper is organized as follow, section 6.3 describes the proposed methodology and subsections further elaborate the vessel reconstruction and bifurcation detection algorithm. Results are discussed in section 6.4. Future work in the proposed algorithm is presented in section 6.5 followed by the acknowledgment in the last section.

6.3   Materials and methods

In this section the preprocessing, Hessian method and the proposed algorithm to detect branch points are discussed. In case of real images of blood vessels multiscale Hessian analysis has been used for vesselness. The vesselness measure drops significantly near the bifurcation points [7]. In the first

step the image is preprocessed that involves the low pass filtering, in our case we used the bandpass filter around the center frequency of the transducer to remove the very high and low frequency components. The filtered signal is further processed using directional Gaussian kernel to enhance the effect of vessels in all directions before applying the Hessian based vessel filtering [19].

6.3.1 Vessel reconstruction

The vascular structure is first enhanced using directional Gaussian function, the ordinary Frangi vessel filtering method uses multiscale Gaussian kernel to enhance the effect of vessels, such multiscale Gaussian kernel is useful to enhance the effect of vessels with varying radii. To maintain the vessels continuity a directional multiscale Gaussian kernel performs better than ordinary Gaussian kernel. In this study we used Gabor wavelet to enhance the effect of vessels in 3D volumetric data [21, 23].

In order to enhance the vascular image, the directional Gabor wavelet is rotated from 0° to 180° with a small step size of 15° and correlate with the image at each angle, the maximum response is preserved. Taking the maximum response from all the images enhanced vascular image is reconstructed.

In the next step, Hessian matrix is calculated at each point in the image or at each voxel point in case of 3D volume data. The detailed analysis of Hessian matrix in case of 3D volume data is discussed here, 2D Hessian matrix can easily be implemented from 3D case. Hessian matrix is calculated by calculating the partial derivatives in three dimensions, which gives the information of the curvature of vascular structures in the volume data. The

hessian matrix can be expressed as

$$H_{(\mathbf{x},s)} = \begin{bmatrix} I_{xx}(\mathbf{x},s) & l_{xy}(\mathbf{x},s) & l_{xz}(\mathbf{x},s) \\ l_{yx}(\mathbf{x},s) & l_{yy}(\mathbf{x},s) & l_{yz}(\mathbf{x},s) \\ l_{zx}(\mathbf{x},s) & l_{zy}(\mathbf{x},s) & l_{zz}(\mathbf{x},s) \end{bmatrix}, \tag{6.1}$$

where $\mathbf{x} = x, y, z$ is the position in 3D volume, lxx are the partial derivatives with respect to x position, lxy is the partial derivative with respect to x and y position respectively and so on. $l(\mathbf{x}, s)$ is the Gaussian filtered image at scale s, s being the standard deviation of the Gaussian function. Eigenvalue decomposition of 3×3 Hessian matrix gives three eigenvalues at each voxel point, which are arranged in increasing order to classify vascular structures. The eigenvalues are calculated at different Gaussian scales in order to extract the vessels with different radii. Frangi et al., [19] defined different ratios to classify vessel like structures, for vessel classification three structures were taken into account plate-like structures, blob and tubular structures. For vessel like structures, two eigenvalues across the vessel are larger than the third which is along the direction of the vessel. In case of plate like structures, one eigenvalue is larger then the two which are along the plate. The ratio in Eq. 6.2 differentiates between vessel and plate like structures.

$$R_A = \frac{|\lambda_2|}{|\lambda_3|}. \tag{6.2}$$

The ratio in Eq. 6.3 differentiates between blob and plate like structures. In case of blob like structures, all the eigenvalues are approximately equal in

magnitude, since blob like structures have high curvature in all directions. The ratio attains value of 1 in case of blob like structures and 0 for other structures.

$$R_B = \frac{|\lambda_1|}{\sqrt{|\lambda_2||\lambda_3|}}. \tag{6.3}$$

Eq. 6.4 shows the Euclidean norm, to control the signal to noise ratio, this term emphasis the areas of high contrast.

$$S = \sqrt{\lambda_1^2 + \lambda_2^2 + \lambda_3^2}. \tag{6.4}$$

The combined ratios are expressed as

$$y(x,s) = \begin{cases} 0, & \lambda_2^2 > 0 \text{ or } \lambda_3^2 > 0 \\ \left(1 - e^{\left(-\frac{R_A^2}{2\alpha^2}\right)}\right) e^{\left(-\frac{R_b^2}{2\beta^2}\right)} \left(1 - e^{\left(-\frac{S^2}{2\gamma^2}\right)}\right) & \text{else,} \end{cases} \tag{6.5}$$

The equation is used to find vessel-like structures, coefficients α, β and γ are used to control the sensitivity for vessel classification, blob like structures and noise respectively. Vesselness is computed at different Gaussian scales and maximum response is preserved at each scale to get the vessel filtered image. Fig. 6.1 (a) shows the vascular image of human finger cuticle. Figs. 6.1 (b) and (c) show the results of ordinary and directional Gaussian kernel on human finger cuticle.
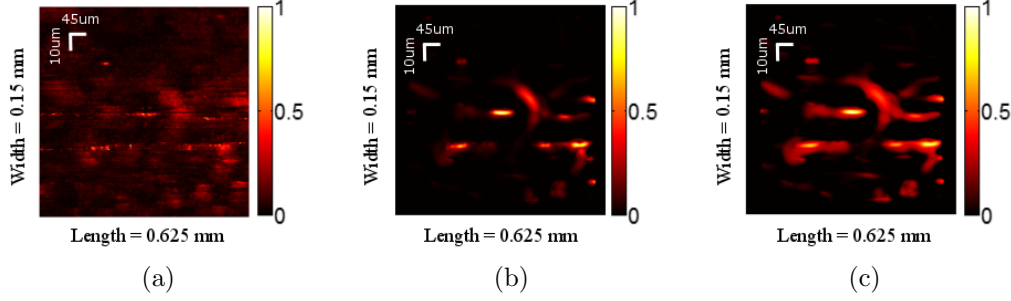
Figure 6.1: Vessel enhancement using Hessian based method; (a) Raw MAP image of human finger cuticle; (b) Filtered vessels using ordinary Gaussian kernel; (c) Filtered image using directional Gaussian kernel.

6.3.2   Bifurcation detection

The proposed algorithm to detect bifurcation points assumes that branch points maintain the rotation symmetry, which means if the branch; a patch containing the branch point is rotated at some angles, then branch point can be seen as a blob like structure in that image patch. However, if the branch point is not in the center of the patch in such case the position of the branch point will be different at different angles. We introduced an equation to detect if there is a branch point in 3D volumetric data. Eq. 6.6 shows the use of 3 eigenvalues to detect branch points. The main steps of the algorithm are described below

$$B = \lambda_{3\mathrm{max}}^2 - \lambda_{1\mathrm{max}} * (t_{max}). * (\lambda_{3\mathrm{max}})^2. * \lambda_{1\mathrm{max}}. * \lambda_{2\mathrm{max}}. \qquad (6.6)$$

$$t_{max} = \lambda_{3\mathrm{max}} - \lambda_{2\mathrm{max}} - \lambda_{1\mathrm{max}}.$$

$\lambda_{1\mathrm{max}}$, $\lambda_{2\mathrm{max}}$ and $\lambda_{3\mathrm{max}}$ are the maximum eigenvalues from multiscale

vessel filtering and t_{max} is the difference of eigenvalues from the maximum eigenvalue.

1. Patch of size $n \times n \times n$ is extracted from λ_{1max}, λ_{2max} and λ_{3max}.

2. Patch is rotated from $0°$ to $180°$ with a step size of $\theta°$ at three different planes x, y and z respectively.

3. Response of Eq. 6.6 is calculated at each angle which results in blob like structure at bifurcation points shown in Fig. 6.3.

4. Blob structures are detected by measuring the eccentricity.

5. Maximum number of overlapping detected blob structures confirms the branch point.

6. Repeat Step 1 to 6 for all the patches of image.

Bifurcation points appear as blob like structure. In the proposed method eccentricity is calculated for all the patches after convolving with Gaussian kernel, which enhances the effect of blob structures. Eccentricity of circular object is ideally 0 which increases as the shape changes. In case of 3D volumetric data we consider eccentricity as the ratio of the length of longer axis to the shorter axis. The eccentricity threshold of 6.5 is considered in our case, below which the structure is considered a blob structure. This threshold is chosen manually which vary from application to application. The enhanced branch points are threshold and re-rotated to $(-\theta°)$. It is shown that the position of the bifurcation points remain the same when re-rotated. Therefore, when all the patches are re-rotated the blob like threshold structures

overlapped at the original bifurcation position. In order to demonstrate that branch points maintain their rotation symmetry, centroid of the re-rotated patches are calculated. The centroid position of the patch at 0° is taken as a reference position and compared with the detected centroid positions of the re-rotated patches. Error is taken as the distance between the reference centroid of branch point to the centroid of branch point when rotated at different angles using Eq. 6.7. The error calculation shows that at which angles branch points are detected. Small values of error show the actual position of branch point. Fig. 6.2 shows the error calculation at different angles from 0° to 360° due to symmetry 0° to 180° is considered in calculation. The error is minimum at 30°, 45°, 105°, 180° etc. Few of the angles where error is maximum are 60°, 225°,240° and 255°. The angles where error is minimum show the actual branch point position.

$$E = \sqrt{(C_{rx} - C_{\theta x}) + (C_{ry} - C_{\theta y}) + (C_{rz} - C_{\theta z})} \tag{6.7}$$

where C_{rx}, C_{ry} and C_{rz} are the coordinates of reference centroid points and $C_{\theta x}$, $C_{\theta y}$ and $C_{\theta z}$ are the detected centroid points at angle θ respectively.

Fig. 6.3 shows the branch points at different angles by the proposed method. Fig. 6.3 (b), (e) and (h) show branch points at 0°, 90° and 180° respectively if the original image is rotated at these angles. Fig. 6.3 (c), (d), (f) and (g) show no circular blobs of branch point and thus neglected. Detection of Bifurcation points using Laplacian and Determinant of Hessian (DoH) [7], are not always guaranteed to find bifurcation points. In case of noisy and low intensity values at bifurcation points, DoH may not perform
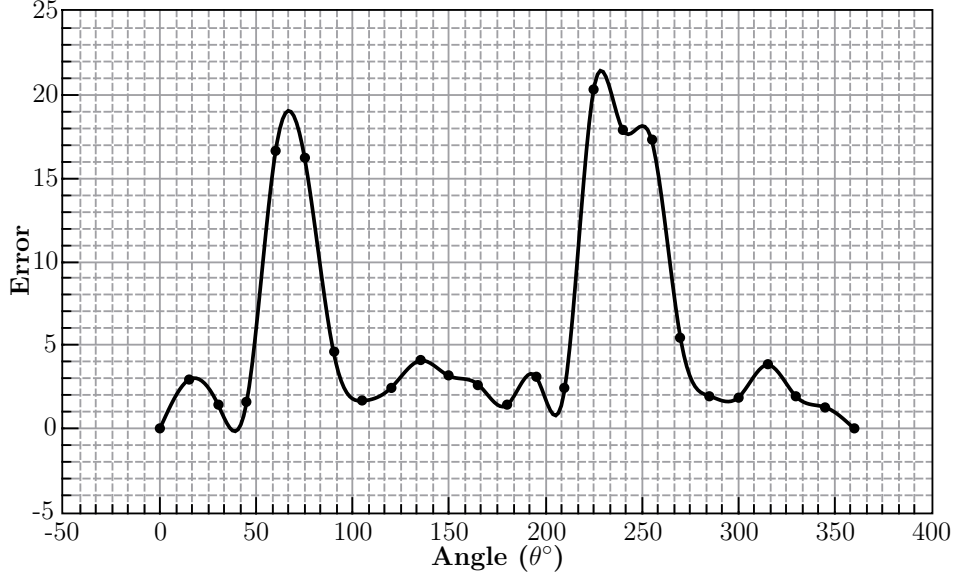
Figure 6.2: Error calculation at different angles.

well. Fig. 6.3 (i) shows DoH, it is easy to calculate at the cost of enhancing the edges point. Fig. 6.4 shows the detected 3D bifurcation point. Fig. 6.4(c) shows the enhanced blob structure after applying the proposed equation 6.6. The image is further processed with a Gaussian function to enhance the effect of blob structures and then threshold as shown in Figs. 6.4e and 6.4f then a blob structure is extracted by a method as discussed in this section.

6.4 Results and discussion

The proposed method is tested on synthetic volumetric data and also on photoacoustic images acquired from OR-PAM. The synthetic data generated using MATLAB R2012b to mimic the real bifurcation point and Im-

(a) Input image   (b) 0°   (c) 15°

(d) 30°   (e) 90°   (f) 135°

(g) 150°   (h) 180°   (i) Determinant of Hessian
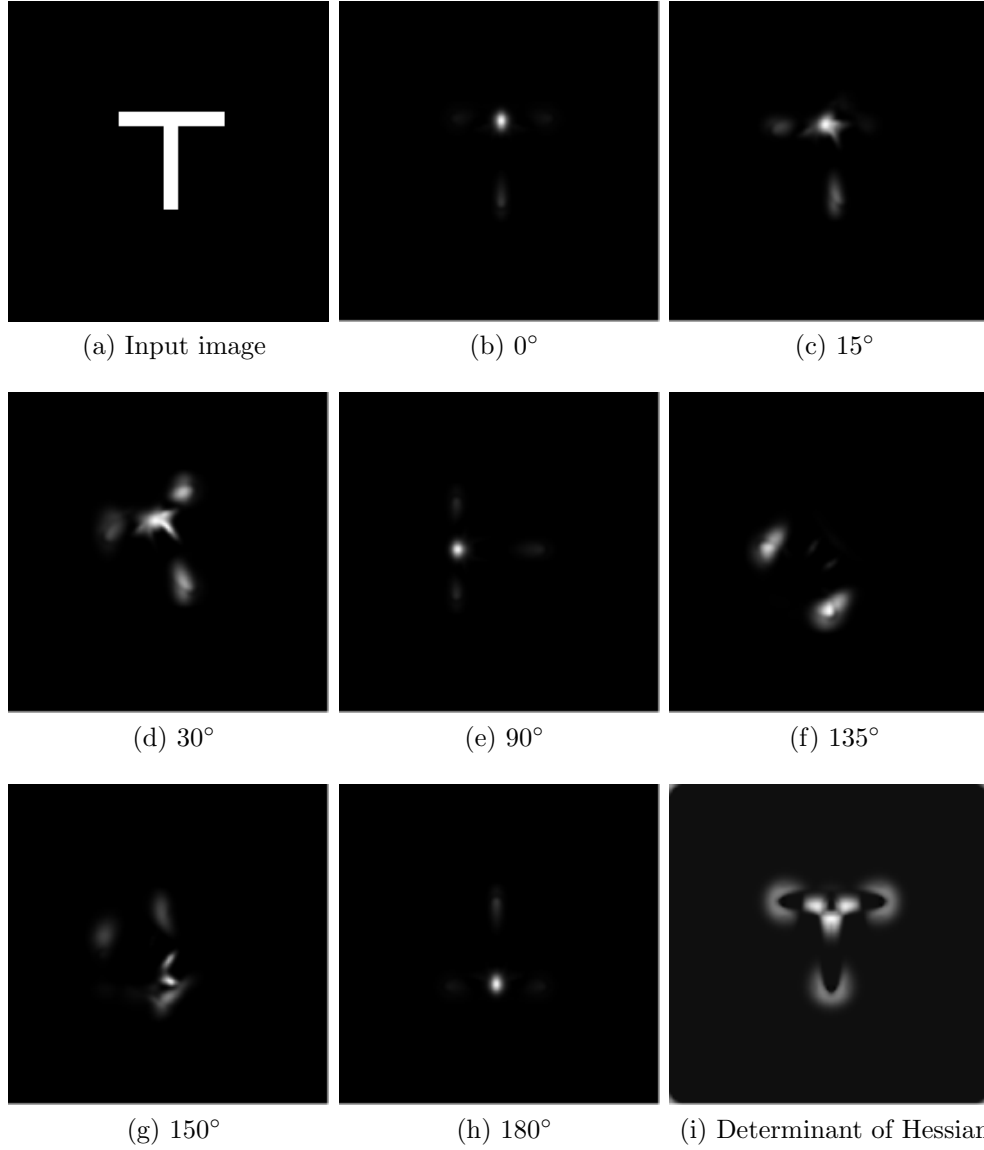
Figure 6.3: (a) Original input image ; (b) - (h) Branch point enhancement at different angles ; (i) Determinant of Hessian.

ageJ was used to visualize 3D volumetric data [60]. To test the capability of the algorithm 3D volumetric data of mouse ear was acquired. The data was acquired through raster scanning of the OR-PAM system. The size of the data was 256×400×400 pixels, 256 is the depth and 400×400 are the

(a) MAP of a bifurcation.

(b) Bmode of a birfurcation.

(c) MAP image after apply-
ing the proposed equation.

(d) Bmode image after ap-
plying the proposed equa-
tion.

(e) Threshold of detected
blob shown in MAP image.

(f) Threshold of detected
blob shown in Bmode image.
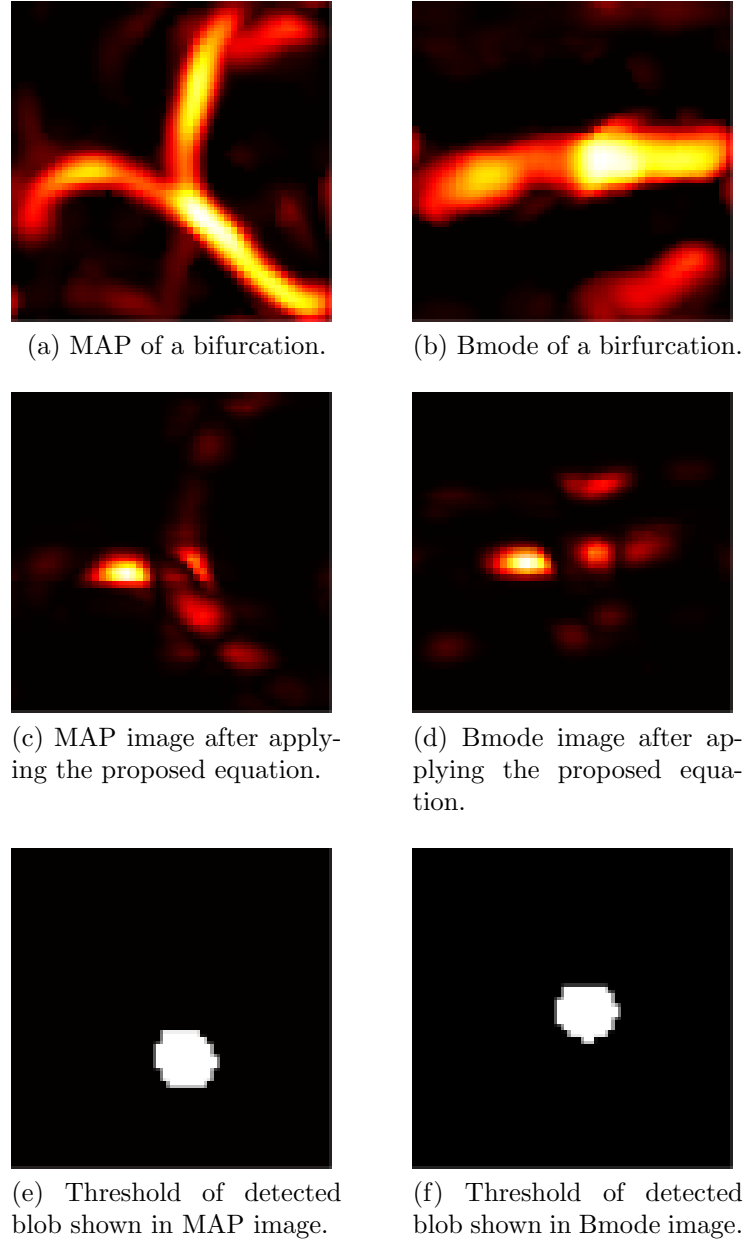
Figure 6.4: Threshold of a bifurcation point.

length and width respectively. To irradiate the tissues laser with a wave-
length of $532\,nm$, pulse duration $8\,ns$ and pulse repetition frequency (PRF)
of $5\,kHz$ was used. (Micro Photo Acoustic Inc. in NY ,USA) and (Advanced

Optowave Corporation, NY, USA). The center frequency of the ultrasonic transducer was 20 MHz. The first experiment in which a PA image of human hair is acquired, two hairs are placed crossing way so a branch point could be make. Fig. 6.6 shows the detected bifurcation point. Fig. 6.6c shows the detected bifurcation point in a 60° rotated image. The experiments performed on mouse were approved by the Ethical Committee Review Board of Tohoku University. For laser safety, standards defined by American National Standards Institute (ANSI) Z136 were followed. Fig. 6.5 shows the detected bifurcation point at different angles shown as a blob like structure. The original position of bifurcation is at 0° as shown in Fig. 6.5 (a) and hence taken as a reference bifurcation position. Fig. 6.5 (b) shows the detected bifurcation at 60° where the position is different as compared to position at 0° and at 105° in Fig. 6.5 (c). Fig. 6.7 shows the bifurcation point on 3D patches of photoacoustic volumetric data. The 3D patches show the different orientations of mouse ear vessels, where the bifurcation point is shown as a blob like structure. Fig. 6.8 (a) shows the 3D vasculature of mouse ear. The total depth of the image is 0.78 mm, width and height are 3.2 mm respectively. Fig. 6.8 (b) shows the detected branch points in 3D vasculature of mouse ear.

6.5   Summary

We showed that bifurcation detection filter can be implemented by using the eigenvalues that are used to filter the vascular structures. It was shown that bifurcation points maintain the rotation symmetry, Our proposed equation
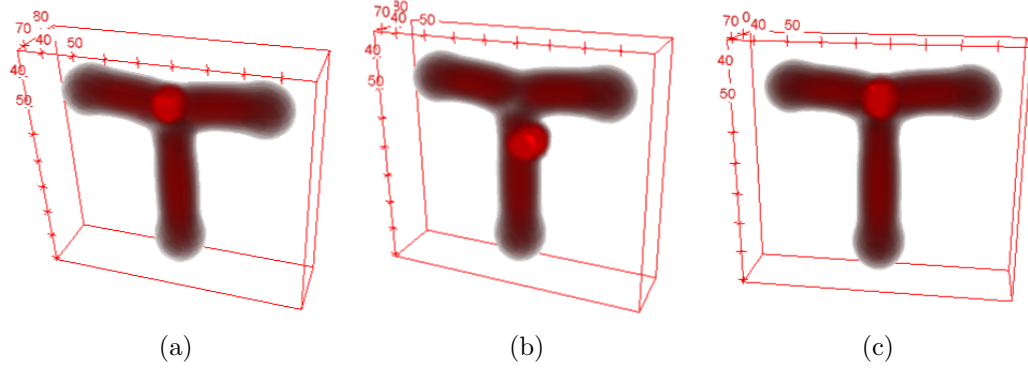
Figure 6.5: (a) Reference bifurcation point ; (b) Branch point detection at 60°; (c) Branch point detection at 105°.
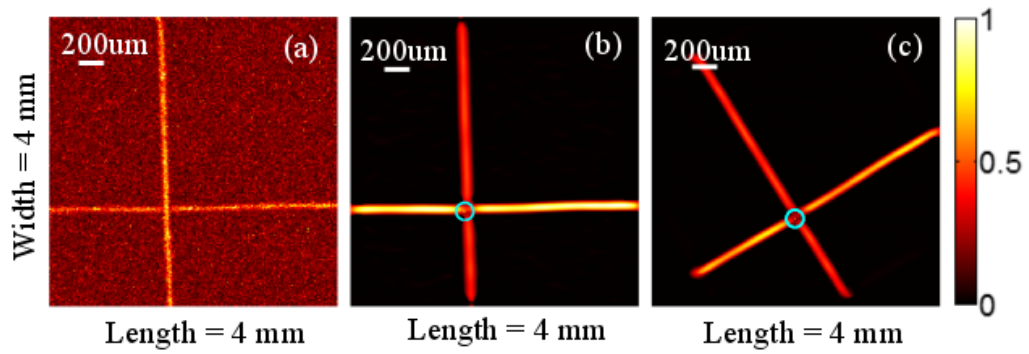
Figure 6.6: (a) Raw image of human hair placed perpendicular to each other ; (b) Denoise and bifurcation point detected on human hair cross point shown in cyan circle ; (c) Detected bifurcation point in rotated image shown in cyan circle.

to find the bifurcation point enhances its effect at some angles, by taking the advantage the image is re-rotated to find the maximum overlapping points in order to find the exact bifurcation position. The proposed algorithm can be improved by removing the limitation of small patches in the image.

(a)   (b)   (c)
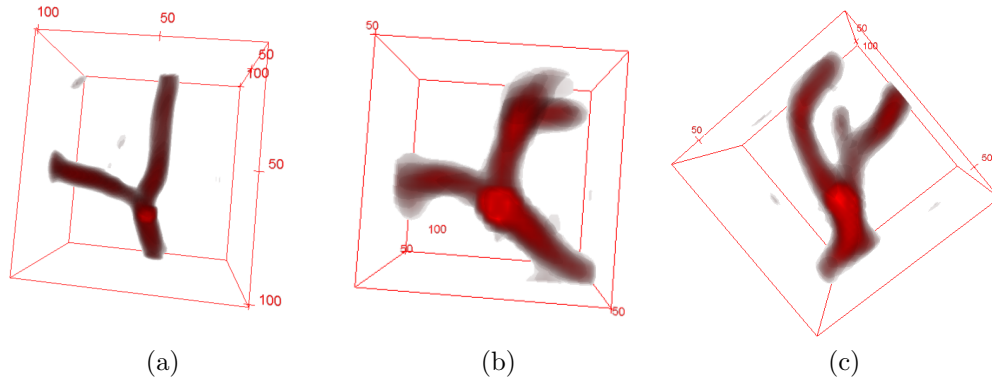
Figure 6.7: (a), (b),(c) Detected bifurcation point in 3D vasculature.

(a)   (b)
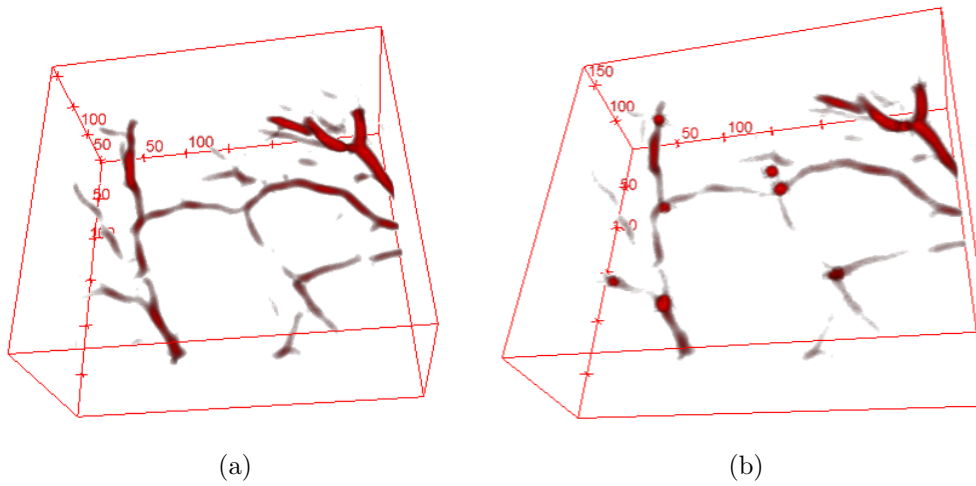
Figure 6.8: (a) 3D vasculature of mouse ear ; (b) Detected bifurcation points
in 3D vasculature of mouse ear.

Chapter 7

Conclusion

This chapter summarizes the contribution of the thesis and discusses avenues for future research. The research discussed in this thesis is based on the vascular studies and their reconstruction for clear visualization. The study of vessels is play an important role for an early diagnosis where its detection is also complicated. Different imaging modalities have been used to extract the vascular structures but each modality has its limitation. In this research we used OR-PAM to extract the vascular structures non-invasive. The study conducted in this research mainly consists of denoising and reconstructing of vascular structures.

The main contribution of this research is

1. Vessel enhancement with 3D Gabor wavelet. This filter has been widely used for 2D images. In this research we make a 3D filter to enhance the vascular effect in 3D images.

2. Integrated method of wavelet and Hessian based filtering is introduced

in this research to classify vascular structures.

3. Spatial filtering methods not always work at junction points of vessels. In this research, we proposed a novel method to detect the bifurcation points in 3D volumetric data which is based on eigenvalues of the Hessian matrix.

4. Compression methods for image denoising have been widely used in different applications like image and video compression, denoising and many more. In this research we used sparse representation based PA image denoising.

The methods proposed in this research show appreciable results to denoise and reconstruct vascular structure.

7.1   Directions for future work

There are still some shortcomings, where the proposed methods need to be modified for better vascular reconstruction.

1. Gabor wavelet enhances the vascular structures but also introduces the smoothness in the image because of dilation parameter. The smoothness in such filter can be minimized by choosing dilatation parameter in an automated way.

2. The Hessian based method classify all the blood vessels but fails at bifurcation and at end points. The method can be improved by modifying the filter in such a way that it consider the junction point as well.

3. The sparse representation based denoising has high computation time for better denoising. This problem can be further minimized by introducing grouping in the data.

References

[1] M. Aharon, M. Elad, and A. Bruckstein. k-svd: An algorithm for designing overcomplete dictionaries for sparse representation. *IEEE Transactions on signal processing*, 54(11):4311–4322, 2006.

[2] B. Al-Diri, A. Hunter, and D. Steel. An active contour model for segmenting and measuring retinal vessels. *IEEE Transactions on Medical imaging*, 28(9):1488–1497, 2009.

[3] G. R. Arce. *Nonlinear signal processing: a statistical approach*. John Wiley & Sons, 2005.

[4] S. Aylward, E. Bullitt, S. Pizer, and D. Eberly. Intensity ridge and widths for tubular object segmentation and description. In *Mathematical Methods in Biomedical Image Analysis, 1996., Proceedings of the Workshop on*, pages 131–138. IEEE, 1996.

[5] S. R. Aylward and E. Bullitt. Initialization, noise, singularities, and scale in height ridge traversal for tubular object centerline extraction. *IEEE transactions on medical imaging*, 21(2):61–75, 2002.

[6] G. Azzopardi and N. Petkov. Automatic detection of vascular bifurcations in segmented retinal images using trainable cosfire filters. *Pattern Recognition Letters*, 34(8):922–933, 2013.

[7] D.-M. Baboiu and G. Hamarneh. Vascular bifurcation detection in scale-space. In *Mathematical Methods in Biomedical Image Analysis (MM-BIA), 2012 IEEE Workshop on*, pages 41–46. IEEE, 2012.

[8] S. Baez. An open cremaster muscle preparation for the study of blood vessels by in vivo microscopy. *Microvascular research*, 5(3):384–394, 1973.

[9] A. Buades, B. Coll, and J.-M. Morel. A review of image denoising algorithms, with a new one. *Multiscale Modeling & Simulation*, 4(2):490–530, 2005.

[10] C. S. Burrus, R. A. Gopinath, and H. Guo. Introduction to wavelets and wavelet transforms: a primer. 1997.

[11] T. T. Cai and L. Wang. Orthogonal matching pursuit for sparse signal recovery with noise. *IEEE Transactions on Information Theory*, 57(7):4680–4688, 2011.

[12] B. Chen, Y. Chen, Z. Shao, T. Tong, and L. Luo. Blood vessel enhancement via multi-dictionary and sparse coding: Application to retinal vessel enhancing. *Neurocomputing*, 200:110–117, 2016.

[13] B. Chiu, M. Egger, J. D. Spence, G. Parraga, and A. Fenster. Quantification of progression and regression of carotid vessel atherosclerosis

using 3d ultrasound images. In *Engineering in Medicine and Biology Society, 2006. EMBS'06. 28th Annual International Conference of the IEEE*, pages 3819–3822. IEEE, 2006.

[14] I. Daubechies. Orthonormal bases of compactly supported wavelets. *Communications on pure and applied mathematics*, 41(7):909–996, 1988.

[15] G. Diebold, T. Sun, and M. Khan. Photoacoustic monopole radiation in one, two, and three dimensions. *Physical review letters*, 67(24):3384, 1991.

[16] G. Diebold, T. Sun, and M. Khan. Photoacoustic waveforms generated by fluid bodies. pages 263–269, 1992.

[17] M. Elad and M. Aharon. Image denoising via sparse and redundant representations over learned dictionaries. *IEEE Transactions on Image processing*, 15(12):3736–3745, 2006.

[18] J. Fitch, E. Coyle, and N. Gallagher. Median filtering by threshold decomposition. *IEEE Transactions on Acoustics, Speech, and Signal Processing*, 32(6):1183–1188, 1984.

[19] A. F. Frangi, W. J. Niessen, K. L. Vincken, and M. A. Viergever. enhancement filtering. In *International Conference on Medical Image Computing and Computer-Assisted Intervention*, pages 130–137. Springer, 1998.

[20] A. F. Frangi, W. J. Niessen, K. L. Vincken, and M. A. Viergever. Multiscale vessel enhancement filtering. In *International Conference on*

Medical Image Computing and Computer-Assisted Intervention, pages 130–137. Springer, 1998.

[21] D. Gabor. Theory of communication. part 1: The analysis of information. *Journal of the Institution of Electrical Engineers-Part III: Radio and Communication Engineering*, 93(26):429–441, 1946.

[22] R. Ha, P. Liu, and K. Jia. An improved adaptive median filter algorithm and its application. In *Advances in Intelligent Information Hiding and Multimedia Signal Processing: Proceeding of the Twelfth International Conference on Intelligent Information Hiding and Multimedia Signal Processing, Nov., 21-23, 2016, Kaohsiung, Taiwan, Volume 2*, pages 179–186. Springer, 2017.

[23] I. U. Haq, R. Nagoaka, T. Makino, T. Tabata, and Y. Saijo. 3d gabor wavelet based vessel filtering of photoacoustic images. In *Engineering in Medicine and Biology Society (EMBC), 2016 IEEE 38th Annual International Conference of the*, pages 3883–3886. IEEE, 2016.

[24] E. R. Hill, W. Xia, M. J. Clarkson, and A. E. Desjardins. Identification and removal of laser-induced noise in photoacoustic imaging using singular value decomposition. *Biomedical Optics Express*, 8(1):68–77, 2017.

[25] S. Hu, K. Maslov, V. Tsytsarev, and L. V. Wang. Functional transcranial brain imaging by optical-resolution photoacoustic microscopy. *Journal of biomedical optics*, 14(4):040503–040503, 2009.

[26] S. Hu, K. Maslov, and L. V. Wang. Second-generation optical-resolution photoacoustic microscopy with improved sensitivity and speed. *Optics letters*, 36(7):1134–1136, 2011.

[27] S. Hu, K. Maslov, and L. V. Wang. Three-dimensional optical-resolution photoacoustic microscopy. In *Biomedical Optical Imaging Technologies*, pages 55–77. Springer, 2013.

[28] S. Hu and L. V. Wang. Photoacoustic imaging and characterization of the microvasculature. *Journal of biomedical optics*, 15(1):011101–011101, 2010.

[29] S. Hu and L. V. Wang. Optical-resolution photoacoustic microscopy: auscultation of biological systems at the cellular level. *Biophysical journal*, 105(4):841–847, 2013.

[30] J.-H. Jang and K.-S. Hong. Detection of curvilinear structures and reconstruction of their regions in gray-scale images. *Pattern Recognition*, 35(4):807–824, 2002.

[31] Z. Jiang, Z. Lin, and L. S. Davis. Learning a discriminative dictionary for sparse coding via label consistent k-svd. In *Computer Vision and Pattern Recognition (CVPR), 2011 IEEE Conference on*, pages 1697–1704. IEEE, 2011.

[32] A. Kazakeviciute, C. J. H. Ho, and M. Olivo. Multispectral photoacoustic imaging artifact removal and denoising using time series model-based spectral noise estimation. *IEEE transactions on medical imaging*, 35(9):2151–2163, 2016.

[33] A. Kerkeni, A. B. Abdallah, A. Manzanera, and M. H. Bedoui. Automatic bifurcation detection in coronary x-ray angiographies. In *Computer Graphics, Imaging and Visualization (CGiV), 2016 13th International Conference on*, pages 333–338. IEEE, 2016.

[34] M. Khan and G. Diebold. The photoacoustic effect generated by an isotropic solid sphere. *Ultrasonics*, 33(4):265–269, 1995.

[35] R. P. Kumar, F. Albregtsen, M. Reimers, B. Edwin, T. Langø, and O. J. Elle. Three-dimensional blood vessel segmentation and centerline extraction based on two-dimensional cross-section analysis. *Annals of biomedical engineering*, 43(5):1223–1234, 2015.

[36] M. Lebrun and A. Leclaire. An implementation and detailed analysis of the k-svd image denoising algorithm. *Image Processing On Line*, 2:96–133, 2012.

[37] T. S. Lee. Image representation using 2d gabor wavelets. *IEEE Transactions on pattern analysis and machine intelligence*, 18(10):959–971, 1996.

[38] M.-L. Li, J.-T. Oh, X. Xie, G. Ku, W. Wang, C. Li, G. Lungu, G. Stoica, and L. V. Wang. Simultaneous molecular and hypoxia imaging of brain tumors in vivo using spectroscopic photoacoustic tomography. *Proceedings of the IEEE*, 96(3):481–489, 2008.

[39] Q. Li, S. Sone, et al. Selective enhancement filters for nodules, vessels, and airway walls in two-and three-dimensional ct scans. *Medical physics*, 30(8):2040–2051, 2003.

[40] L. M. Lorigo, O. Faugeras, W. E. L. Grimson, R. Keriven, R. Kikinis, A. Nabavi, and C.-F. Westin. Codimension-two geodesic active contours for the segmentation of tubular structures. In *Computer Vision and Pattern Recognition, 2000. Proceedings. IEEE Conference on*, volume 1, pages 444–451. IEEE, 2000.

[41] L. M. Lorigo, O. D. Faugeras, W. E. L. Grimson, R. Keriven, R. Kikinis, A. Nabavi, and C.-F. Westin. Curves: Curve evolution for vessel segmentation. *Medical image analysis*, 5(3):195–206, 2001.

[42] C. Lutzweiler, S. Tzoumas, A. Rosenthal, V. Ntziachristos, and D. Razansky. High-throughput sparsity-based inversion scheme for optoacoustic tomography. *IEEE transactions on medical imaging*, 35(2):674–684, 2016.

[43] M. R. Lyaker, D. B. Tulman, G. T. Dimitrova, R. H. Pin, and T. J. Papadimos. Arterial embolism. *International journal of critical illness and injury science*, 3(1):77, 2013.

[44] J. Mairal, F. Bach, J. Ponce, et al. Sparse modeling for image and vision processing. *Foundations and Trends® in Computer Graphics and Vision*, 8(2-3):85–283, 2014.

[45] S. Mallat. *A wavelet tour of signal processing: the sparse way*. Academic press, 2008.

[46] K. Maslov, G. Stoica, and L. V. Wang. In vivo dark-field reflection-mode photoacoustic microscopy. *Optics letters*, 30(6):625–627, 2005.

[47] K. Maslov, H. F. Zhang, S. Hu, and L. V. Wang. Optical-resolution photoacoustic microscopy for in vivo imaging of single capillaries. *Optics letters*, 33(9):929–931, 2008.

[48] D. Maton, J. Hopkins, W. McLaughlin Ch, S. Johnson, M. Warner, D. LaHart, J. Wright, and D. Kulkarni. Human biology and health. englewood cliffs, new jersey, us. *Prentice Hall. ISBN 0-13-981176-1. OCLC*, 32308337:1993, 1997.

[49] C. McIntosh and G. Hamarneh. Vessel crawlers: 3d physically-based deformable organisms for vasculature segmentation and analysis. In *Computer Vision and Pattern Recognition, 2006 IEEE Computer Society Conference on*, volume 1, pages 1084–1091. IEEE, 2006.

[50] S. Oladipupo, S. Hu, J. Kovalski, J. Yao, A. Santeford, R. E. Sohn, R. Shohet, K. Maslov, L. V. Wang, and J. M. Arbeit. Vegf is essential for hypoxia-inducible factor-mediated neovascularization but dispensable for endothelial sprouting. *Proceedings of the National Academy of Sciences*, 108(32):13264–13269, 2011.

[51] T. Oruganti, J. G. Laufer, and B. E. Treeby. Vessel filtering of photoacoustic images. In *Proc. SPIE*, volume 8581, page 85811W, 2013.

[52] T. N. Pappas and J. S. Lim. A new method for estimation of coronary artery dimensions in angiograms. *IEEE Transactions on Acoustics, Speech, and Signal Processing*, 36(9):1501–1513, 1988.

[53] V. Prinet, O. Monga, C. Ge, S. Xie, and S. Ma. Thin network extraction in 3d images: application to medical angiograms. In *Pattern*

Recognition, 1996., Proceedings of the 13th International Conference on, volume 3, pages 386–390. IEEE, 1996.

[54] X. Qian, M. P. Brennan, D. P. Dione, W. L. Dobrucki, M. P. Jackowski, C. K. Breuer, A. J. Sinusas, and X. Papademetris. A non-parametric vessel detection method for complex vascular structures. *Medical image analysis*, 13(1):49–61, 2009.

[55] R. Rubinstein, M. Zibulevsky, and M. Elad. Efficient implementation of the k-svd algorithm using batch orthogonal matching pursuit. *Cs Technion*, 40(8):1–15, 2008.

[56] Y. Sato, S. Nakajima, H. Atsumi, T. Koller, G. Gerig, S. Yoshida, and R. Kikinis. 3d multi-scale line filter for segmentation and visualization of curvilinear structures in medical images. In *CVRMed-MRCAS'97*, pages 213–222. Springer, 1997.

[57] Y. Sato, S. Nakajima, N. Shiraga, H. Atsumi, S. Yoshida, T. Koller, G. Gerig, and R. Kikinis. Three-dimensional multi-scale line filter for segmentation and visualization of curvilinear structures in medical images. *Medical image analysis*, 2(2):143–168, 1998.

[58] E. V. Savateeva, A. A. Karabutov, S. V. Solomatin, and A. A. Oraevsky. Optical properties of blood at various levels of oxygenation studied by time-resolved detection of laser-induced pressure profiles. In *International Symposium on Biomedical Optics*, pages 63–75. International Society for Optics and Photonics, 2002.

[59] C. A. Schneider, W. S. Rasband, and K. W. Eliceiri. Nih image to imagej: 25 years of image analysis. *Nature methods*, 9(7):671, 2012.

[60] C. A. Schneider, W. S. Rasband, and K. W. Eliceiri. Nih image to imagej: 25 years of image analysis. *Nature methods*, 9(7):671, 2012.

[61] M. Schneider, S. Hirsch, B. Weber, G. Székely, and B. H. Menze. Joint 3-d vessel segmentation and centerline extraction using oblique hough forests with steerable filters. *Medical image analysis*, 19(1):220–249, 2015.

[62] M. Sivaramakrishnan, K. Maslov, H. F. Zhang, G. Stoica, and L. V. Wang. Limitations of quantitative photoacoustic measurements of blood oxygenation in small vessels. *Physics in medicine and biology*, 52(5):1349, 2007.

[63] M. Sofka and C. V. Stewart. Retinal vessel centerline extraction using multiscale matched filters, confidence and edge measures. *IEEE transactions on medical imaging*, 25(12):1531–1546, 2006.

[64] B. Soroushian, W. M. Whelan, and M. C. Kolios. Study of laser-induced thermoelastic deformation of native and coagulated ex-vivo bovine liver tissues for estimating their optical and thermomechanical properties. *Journal of biomedical optics*, 15(6):065002–065002, 2010.

[65] Springer. *Statistical 3D vessel segmentation using a Rician distribution*, 1999.

[66] M. Storath and A. Weinmann. Fast median filtering for phase or orientation data. *IEEE Transactions on Pattern Analysis and Machine Intelligence*, 2017.

[67] J. A. Tropp and A. C. Gilbert. Signal recovery from random measurements via orthogonal matching pursuit. *IEEE Transactions on information theory*, 53(12):4655–4666, 2007.

[68] C. Xiao, M. Staring, D. Shamonin, J. H. Reiber, J. Stolk, and B. C. Stoel. A strain energy filter for 3d vessel enhancement with application to pulmonary ct images. *Medical image analysis*, 15(1):112–124, 2011.

[69] Y. Xu, J. B. Weaver, D. M. Healy, and J. Lu. Wavelet transform domain filters: a spatially selective noise filtration technique. *IEEE transactions on image processing*, 3(6):747–758, 1994.

[70] J. Yang, S. Ma, Q. Sun, W. Tan, M. Xu, N. Chen, and D. Zhao. Improved hessian multiscale enhancement filter. *Bio-medical materials and engineering*, 24(6):3267–3275, 2014.

[71] D.-K. Yao, C. Zhang, K. Maslov, and L. V. Wang. Photoacoustic measurement of the grüneisen parameter of tissue. *Journal of biomedical optics*, 19(1):017007–017007, 2014.

[72] J. Yao, A. A. Kaberniuk, L. Li, D. M. Shcherbakova, R. Zhang, L. Wang, G. Li, V. V. Verkhusha, and L. V. Wang. Multiscale photoacoustic tomography using reversibly switchable bacterial phytochrome as a near-infrared photochromic probe. *Nature methods*, 13(1):67–73, 2016.

[73] J. Yao, L. Wang, J.-M. Yang, K. I. Maslov, T. T. Wong, L. Li, C.-H. Huang, J. Zou, and L. V. Wang. High-speed label-free functional photoacoustic microscopy of mouse brain in action. *Nature methods*, 12(5):407–410, 2015.

[74] L. Yao and H. Jiang. Enhancing finite element-based photoacoustic tomography using total variation minimization. *Applied Optics*, 50(25):5031–5041, 2011.

[75] C. Yeh, B. Soetikno, S. Hu, K. I. Maslov, and L. V. Wang. Microvascular quantification based on contour-scanning photoacoustic microscopy. *Journal of biomedical optics*, 19(9):096011–096011, 2014.

[76] C. Zhang, K. Maslov, and L. V. Wang. Subwavelength-resolution label-free photoacoustic microscopy of optical absorption in vivo. *Optics letters*, 35(19):3195–3197, 2010.

[77] C. Zhang, K. Maslov, J. Yao, and L. V. Wang. In vivo photoacoustic microscopy with 7.6-μm axial resolution using a commercial 125-mhz ultrasonic transducer. *Journal of biomedical optics*, 17(11):116016–116016, 2012.

[78] C. Zhang, Y. Zhou, C. Li, and L. V. Wang. Slow-sound photoacoustic microscopy. *Applied physics letters*, 102(16):163702, 2013.

[79] H. F. Zhang, K. Maslov, M. Sivaramakrishnan, G. Stoica, and L. V. Wang. Imaging of hemoglobin oxygen saturation variations in single vessels in vivo using photoacoustic microscopy. *Applied physics letters*, 90(5):053901, 2007.

[80] H. F. Zhang, K. Maslov, G. Stoica, and L. V. Wang. Functional photoacoustic microscopy for high-resolution and noninvasive in vivo imaging. *Nature biotechnology*, 24(7):848–851, 2006.

[81] H. F. Zhang, K. Maslov, and L. V. Wang. In vivo imaging of subcutaneous structures using functional photoacoustic microscopy. *Nature protocols*, 2(4):797–804, 2007.

[82] H. Zhao, D. Gao, M. Wang, and Z. Pan. Real-time weighted median filtering with the edge-aware 4d bilateral grid. In *International Conference on Technologies for E-Learning and Digital Entertainment*, pages 125–135. Springer, 2016.

[83] J. Zhou, S. Chang, D. Metaxas, and L. Axel. Vascular structure segmentation and bifurcation detection. In *Biomedical Imaging: From Nano to Macro, 2007. ISBI 2007. 4th IEEE International Symposium on*, pages 872–875. IEEE, 2007.

[84] Y. Zhou and L. V. Wang. Translational photoacoustic microscopy. In *Frontiers in Biophotonics for Translational Medicine*, pages 47–73. Springer, 2016.

Appendix A

Publications

This research activity has led to several publications in international journals and conferences. These are summarized below.

A.0.1 International Journals

1. **Israr Ul haq**, Usman Akram, Yoshifumi Saijo, "Detection of Abnormal Blood Vessels on Optic Disc for Diagnosis of Proliferative Diabetic Retinopathy", *Journal of the Institute of Industrial Applications Engineers*, Vol.3, No.1, pp. 1−5, Jan. 2015.

2. **Israr Ul Haq**, Ryo Nagaoka, Syahril Siregar, Yoshifumi Saijo, "Sparse representation based denoising of photoacoustic images", *Biomedical Physics & Engineering Express*, Volume 3, Number 4, June 2017.

A.0.2 Conference Proceedings

1. **Israr Ul haq**, Usman Akram, Yoshifumi Saijo, "Automated Detection of New Vessels for Classification of Proliferative Diabetic Retinopathy", *Pro-*

ceedings of the 2nd International Conference on Intelligent Systems and Image Processing, Japan, Sept. 2014.

2. **Israr Ul Haq**, Ryo Nagoaka, Takahiro Makino, Takuya Tabata and Yoshifumi Saijo, "3D Gabor Wavelet based Vessel Filtering of Photoacoustic Images",*The 38th Annual International Conference of the IEEE Engineering in Medicine and Biology Society*, Orlando, USA, Aug. 2016.

3. **Israr Ul Haq**, Ryo Nagaoka, Syahril Siregar, and Yoshifumi Saijo, "Vascular Bifurcation Detection by Eigenvalues Analysis", *8th International Conference of Pattern Recognition Systems*, Madrid, Spain, July 2017.

A.0.3   Presentations

1. **Israr Ul Haq**, Usman Akram, Yoshifumi Saijo, "Automated Detection of Optic Disc using Vessels Tracking", *The 53rd Annual Conference of Japanese Society for Medical and Biological Engineering*, Sendai, Japan, June 2014.

2. **Israr Ul Haq**, "Detection of Abnormal Blood Vessels on Optic Disc for Diagnosis of Proliferative Diabetic Retinopathy", The 13th International Symposium on Advanced Biomedical Ultrasound, Sendai, Japan, Oct 2015.

3. **Israr Ul Haq**, "Wavelet based Vessel Filtering of Photoacoustic Images", *The 1st [ImPACT] Symposium on Photoacoustic Imaging and Bio-Medical Imaging for Vascular Health Science*, Japan, Jan. 2016.

4. **Israr Ul Haq**, "Vessel Filtering and Reconstruction of 3D Photoacoustic Images", *10th International Symposium on Medical, Bio- and Nano-Electronics*, Sendai - Japan, March 2016.

5. **Israr Ul Haq**, "Denoising and Reconstruction of Vasculature in Optical Resolution Photoacoustic Microscopy Imaging", *3rd Case Western Reserve University- Tohoku Joint Workshop*, Collaboration on Data Science Engineering, Sendai-Japan, Aug. 2016.

6. **Israr Ul Haq**, "Three-dimensional Vascular Reconstruction in Optical Resolution Photoacoustic Microscopy Imaging", *11th International Workshop on Biomaterials in Interface Science*, Sept. 2016. Sendai-Japan.

7. **Israr Ul Haq**, Ryo Nagaoka, Syahril Siregar, Yoshifumi Saijo, "Vascular Reconstruction in Optical Resolution Photoacoustic Microscopy using Wavelet and Hessian based Method", *Joint Research Society Meeting on Bio-ultrasonic and Photoacoustic Imaging.* Nov. 2016, Shizouka. Japan.

8. **Israr Ul Haq**, Ryo Nagaoka, Syahril Siregar, Yoshifumi Saijo, "Reconstruction of vasculature in optical resolution photoacoustic microscopy using wavelet and hessian based method", *5th Joint Meeting of the Acoustical Society of America and Acoustical Society of Japan*, Nov. 2016 Honolulu, Hawaii, (Oral).